



Global Biogeochemical Cycles

RESEARCH ARTICLE

10.1029/2019GB006460

Key Points:

- Iron fertilization leads to silicic acid leakage if the Si:P uptake ratio decreases sharply enough to overwhelm increased diatom growth
- Silicic acid leakage increases low-latitude opal export, while the Southern Ocean dominates increases in diatom organic matter export
- Silicic acid leakage in response to iron fertilization produces isotopically lighter biogenic opal flux

Correspondence to:

M. Holzer,
mholzer@unsw.edu.au

Citation:

Holzer, M., Pasquier, B., DeVries, T., & Brzezinski, M. A. (2019). Diatom physiology controls silicic acid leakage in response to iron fertilization. *Global Biogeochemical Cycles*, 33. <https://doi.org/10.1029/2019GB006460>

Received 24 OCT 2019

Accepted 21 NOV 2019

Accepted article online 5 DEC 2019

Diatom Physiology Controls Silicic Acid Leakage in Response to Iron Fertilization

Mark Holzer¹, Benoit Pasquier², Timothy DeVries³, and Mark Brzezinski⁴

¹Department of Applied Mathematics, School of Mathematics and Statistics, University of New South Wales, Sydney, New South Wales, Australia, ²Department of Earth System Sciences, University of California, Irvine, CA, USA, ³Earth Research Institute and Department of Geography, University of California, Santa Barbara, CA, USA, ⁴Department of Ecology, Evolution and Marine Biology, The Marine Science Institute, University of California, Santa Barbara, CA, USA

Abstract We explore how the iron dependence of the Si:P uptake ratio $R^{\text{Si:P}}$ of diatoms controls the response of the global silicon cycle and phytoplankton community structure to Southern Ocean iron fertilization. We use a data-constrained model of the coupled Si-P-Fe cycles that features a mechanistic representation of nutrient colimitations for three phytoplankton classes and that is embedded in a data-assimilated global ocean circulation model. We consider three parameterizations of the iron dependence of $R^{\text{Si:P}}$, all of which are consistent with the available field data and allow equally good fits to the observed nutrient climatology but result in very different responses to iron fertilization: Depending on how sharply $R^{\text{Si:P}}$ decreases with increasing iron concentration, iron fertilization can either cause enhanced silicic acid leakage from the Southern Ocean or strengthened Southern Ocean silicon trapping. Enhanced silicic acid leakage occurs if decreases in $R^{\text{Si:P}}$ win over increases in diatom growth, while the converse causes strengthened Southern Ocean silicon trapping. Silicic acid leakage drives a floristic shift in favor of diatoms in the subtropical gyres and stimulates increased low-latitude opal export. The diatom contribution to global phosphorus export increases, but the lower diatom silicon requirement under iron-replete conditions reduces the global opal export. Regardless of $R^{\text{Si:P}}$ parameterization, the global response of the biological phosphorus and silicon pumps is dominated by the Southern Ocean. The Si isotope signature of opal flux becomes systematically lighter with increasing iron-induced silicic acid leakage, consistent with sediment records from iron-rich glacial periods.

1. Introduction

The dominance of the Southern Ocean in the global marine silicon cycle (e.g., Tréguer, 2014) is the result of diatoms efficiently stripping silicon out of upwelled deep waters, which short-circuits much of the silicic acid leakage from the Southern Ocean carried by mode waters. The sinking biogenic silica dissolves in upwelling deep waters, completing the Southern Ocean silicon trap (Holzer et al., 2014). The strong silicon trap of the present-day Southern Ocean results in mode waters that are depleted in silicic acid ($\text{Si}(\text{OH})_4$) but replete in nitrate and phosphate (PO_4). Because these mode waters are an important source of nutrients for low-latitude productivity (Holzer & Primeau, 2013; Sarmiento et al., 2004) their skewed Si:N:P composition limits the contribution of diatoms to biological productivity across much of the world ocean.

Iron limitation plays a key role in the Southern Ocean silicon trap because iron has two opposing influences on diatom physiology: On one hand, iron stress tends to increase silicic acid uptake and hence trapping by raising the diatom Si:N uptake ratio (e.g., Franck et al., 2000; Hutchins & Bruland, 1998; Takeda, 1998; Timmermans et al., 2004), while on the other hand iron stress reduces growth, which tends to reduce silicic acid uptake promoting leakage to low latitudes. The central focus of this paper is on how the iron dependence of the Si:N uptake ratio controls the competition between these opposing factors, thereby shaping the response of the global silicon cycle to iron fertilization. A key aspect of that response, heretofore not fully explored, is that iron fertilization increases Southern Ocean phosphorus trapping (Primeau et al., 2013) so that any increases in silicic acid at low latitudes will be counteracted by reductions in phosphate and nitrate.

While our goal here is to investigate the impacts of iron fertilization on global export production and the role of diatoms in the modern ocean, much of the literature debate on silicic acid leakage has focused on paleoceanography. Decreased silicic acid uptake in response to increased iron input is key to the silicic acid leakage hypothesis (SALH, Brzezinski et al., 2002; Nozaki & Yamamoto, 2001; Matsumoto et al., 2002). The

SALH postulates that an enhanced supply of silicic acid to low latitudes during glacial times favored diatom production at the expense of calcifying plankton, which would change the $\text{CaCO}_3/\text{C}_{\text{org}}$ rain ratio, leading to adjustments in alkalinity and a drawdown of atmospheric CO_2 . The literature is mixed regarding support for the SALH. For example, Bradtmiller et al. (2006) and Kienast et al. (2006) used sediment data from the equatorial Pacific to infer opal fluxes that were not elevated during the last glacial period, contrary to the SALH. Crosta et al. (2007) argued that weakened mode- and intermediate-water formation counteracted reduced Southern Ocean silicic acid uptake, and Dubois et al. (2010) emphasized low-latitude iron input as a control on opal preservation. Other studies provided evidence of the leakage aspect of the SALH in the form of greater silicic acid availability and opal accumulation in the Atlantic, Pacific, and Subarctic during glacial periods (Arellano-Torres et al., 2011; Bradtmiller et al., 2007; Griffiths et al., 2013; Maier et al., 2015; Pichevin et al., 2009). However, silicic acid leakage appears to have been most pronounced during glacial terminations when atmospheric CO_2 levels were already rising suggesting that the effect of leakage on CO_2 drawdown was overshadowed by other processes (Hendry & Brzezinski, 2014).

The inherent uncertainties associated with sparse proxy data and the complexity of their interpretation underscore the importance of modeling. In addition to the box-model studies of Matsumoto et al. (2002) and Matsumoto and Sarmiento (2008), Matsumoto et al. (2014) used a dynamical coarse-resolution Earth system model to explore changes in iron input as well as changes in westerly winds and sea ice as mechanisms for silicic acid leakage. However, all these studies used essentially the same parameterization of the Si:N uptake ratio, and box models or tuned forward models were employed.

In our investigations, we use a data-constrained model of the coupled Fe-P-Si cycles (Pasquier & Holzer, 2017, 2018) that is embedded in a data-assimilated steady circulation representative of the modern climatology (Primeau et al., 2013). To explore the control that diatom physiology exerts on the biogeochemical response to Southern Ocean iron fertilization, we employ three parameterizations of the iron dependence of the Si:N uptake ratio, all of which are consistent with the available field data (assuming constant N:P stoichiometry for diatom communities). In contrast to previous modeling studies that exclusively found enhanced silicic acid leakage in response to Southern Ocean iron fertilization (e.g., Matsumoto & Sarmiento, 2008; Matsumoto et al., 2002, 2014), we find that iron fertilization can lead to either increased Southern Ocean silicon trapping or increased silicic acid leakage, depending on how the diatom Si:N uptake ratio varies with the concentration of dissolved iron (DFe). The degree of silicic acid trapping or leakage is correlated with the $\delta^{30}\text{Si}$ signature of exported opal, highlighting the utility of Si isotope proxy records for constraining past changes in the ocean's silicon cycle.

2. The Nutrient Model

2.1. Key Model Features

The nutrient model is described in detail by Pasquier and Holzer (2017); here we only mention the key features relevant to this study. The model considers three phytoplankton functional classes (diatoms, nanoplankton, and picoplankton, referred to by Pasquier and Holzer (2017) as the diatom, “large,” and “small” classes) and three nutrients: PO_4 , $\text{Si}(\text{OH})_4$, and DFe. The distribution of each phytoplankton functional class has been constrained by satellite retrievals of size classes (Kostadinov et al., 2016), assuming all microplankton are diatoms, and by the percentage of the total export due to each class as estimated from satellite data by Uitz et al. (2010). The biological uptake rate of each nutrient by phytoplankton class c is keyed to its PO_4 uptake rate, U_c^{P} , which is by definition also the growth rate of class c . The phytoplankton concentrations p_c of the three classes are predicted implicitly based on an underlying steady-state logistic model. The growth rate of class c , in units of phosphate uptake rate per unit seawater volume, takes the form

$$U_c^{\text{P}} = \frac{p_c^{\text{max}}}{\tau_c} e^{\kappa T} (F_{\text{L},c} F_{\text{N},c})^2, \quad (1)$$

where parameter p_c^{max} sets the maximum possible value of p_c , τ_c is the growth timescale, $e^{\kappa T}$ models the temperature (T) dependence, and $F_{\text{L},c}$ and $F_{\text{N},c}$ are the light and nutrient limitations, respectively. For diatoms, the nutrient limitation $F_{\text{N},\text{dia}}$ is modeled as the product of three Monod terms of the form $\chi_n / (\chi_n + k_{n,\text{dia}})$, where χ_n is the concentration of the n th nutrient and $k_{n,\text{dia}}$ is the corresponding half-saturation constant. For the picoplankton and nanoplankton classes, $F_{\text{N},c}$ is the product of only phosphate and iron Monod terms. (During model development, we also used the minimum of the three nutrient Monod terms, Liebig's law, e.g., Saito et al., 2008, but found little difference in the optimized solutions and hence used the simpler

multiplicative form.) Most biogeochemical model parameters were objectively optimized by minimizing the mismatch with observed macronutrient concentrations from the World Ocean Atlas (WOA13, Garcia et al., 2014), observed DFe concentrations from GEOTRACES (Mawji et al., 2015) and an earlier data compilation (Tagliabue et al., 2012), and with the logarithm of phytoplankton concentrations as estimated from satellite (Kostadinov et al., 2016).

The silicon cycle is modeled similarly to the work of Holzer et al. (2014), except that the silicic acid uptake rate per unit volume U^{Si} is explicitly keyed to the diatom growth rate $U_{\text{dia}}^{\text{P}}$ through the Si:P uptake ratio, that is,

$$U^{\text{Si}} = R^{\text{Si:P}} U_{\text{dia}}^{\text{P}}, \quad (2)$$

where $U_{\text{dia}}^{\text{P}}$ is given by (1), thus coupling the silicon cycle to the phosphate and iron cycles. The Si:P uptake ratio $R^{\text{Si:P}}$ depends explicitly on the ambient DFe and silicic acid concentrations; we consider three possible parameterizations of this dependency below in section 3. The dissolution of biogenic opal is temperature dependent and follows the formulation of Gnanadesikan (1999), except that the subgrid topography is parameterized so that the fraction of the opal flux intersected by subgrid topography in every grid box is locally dissolved there. As in the formulation of Holzer et al. (2014), opal is not permanently buried (allowing us to neglect external sources) but the flux onto the sediments and its Si isotope signature can readily be diagnosed.

The model's iron cycle was analyzed in detail by Pasquier and Holzer (2017, 2018). The iron cycle is not central to our analysis here and provides primarily a means for supplying DFe to phytoplankton. Because of large uncertainties in the external iron sources, Pasquier and Holzer (2017) generated a family of optimal solutions corresponding to a wide range of different iron source strengths. All family members fit the available phosphate and silicic acid climatologies about equally well. Here we take as our unperturbed base state the “typical” state of that family, which corresponds to aeolian, sedimentary, and hydrothermal iron sources of 5.3, 1.7, and 0.9 Gmol Fe/yr, respectively. The details of the response to iron perturbations do depend on the total iron source, with higher-source states being less sensitive to perturbations than lower-source states, but a detailed quantification of how the response depends on the iron cycle of the base state is beyond the scope of this study.

2.2. Iron Fertilization Perturbations

We focus on idealized Southern Ocean iron fertilization, which consists of adding DFe at a spatially uniform rate to the ocean surface south of 42°S. We use iron additions up to 30 Gmol Fe/yr (roughly 4 times the total global iron source of the unperturbed state). For all Si:P parameterizations considered (details in next section), the DFe concentration averaged over the Southern Ocean euphotic zone (denoted as SO DFe from here on) has a value of ~0.16 nM for our base state and doubles to roughly 0.3 nM for an additional Southern Ocean source of 4 Gmol Fe/yr. When 30 Gmol Fe/yr is added to the Southern Ocean, the SO DFe concentration increases only to ~0.5 nM because the increasing production also increases iron scavenging by organic particles. (Figure A1 of Appendix A shows the SO DFe concentration as a function of the additional Southern Ocean iron source strength.) We have also investigated globally uniform additions of iron to the surface, but when comparing states at the same SO DFe concentration, the responses are qualitatively similar, although there are of course quantitative differences especially in the Northern Hemisphere. (For globally uniform iron fertilization, an additional source of ~18 Gmol Fe/yr is required for a doubling of SO DFe.)

3. Si:P Parameterizations

In our model, the Si:P uptake ratio, $R^{\text{Si:P}}$, plays the role of the Si:N uptake ratio to which it can be compared assuming a constant N:P ratio for diatoms (Quigg et al., 2003; Weber & Deutsch, 2010). High Si:N uptake ratios in iron-stressed diatom communities have a variety of causes including physiological changes within species (Franck et al., 2000; Takeda, 1998; Timmermans et al., 2004) and changes in diatom community composition (Assmy et al., 2013; Marchetti et al., 2010).

The dependence of $R^{\text{Si:P}}$ on the ambient DFe and Si(OH)_4 concentrations χ_{Fe} and χ_{Si} was parameterized by Pasquier and Holzer (2017) as

$$R^{\text{Si:P}} = R_{\text{min}}^{\text{Si}} + (R_{\text{max}}^{\text{Si}} - R_{\text{min}}^{\text{Si}}) \left(\frac{\chi_{\text{Si}}}{\chi_{\text{Si}} + k_{\text{Si:P}}^{\text{Si}}} \right) \left(\frac{k_{\text{Si:P}}^{\text{Fe}}}{\chi_{\text{Fe}} + k_{\text{Si:P}}^{\text{Fe}}} \right). \quad (3)$$

In (3), the parameters $R_{\text{min}}^{\text{Si}}$ and $R_{\text{max}}^{\text{Si}}$ set the minimum and maximum values of $R^{\text{Si:P}}$, the dependence on silicic acid concentration χ_{Si} is assumed to have a simple Monod form with half saturation constant $k_{\text{Si:P}}^{\text{Si}}$, and the parameter $k_{\text{Si:P}}^{\text{Fe}}$ limits the hyperbolic dependence on iron concentration χ_{Fe} to its maximum of unity when $\chi_{\text{Fe}} = 0$. (Note that $k_{\text{Si:P}}^{\text{Fe}}$ and $k_{\text{Si:P}}^{\text{Si}}$ are distinct from the half-saturation constants for diatom growth.) This form of $R^{\text{Si:P}}$ captures reduced silicification in silicon-poor waters as observed by Paasche (1973) (although Marchetti & Harrison, 2007, argue for constant Si levels in the cell when iron is low) and elevated Si:N uptake ratios in iron-depleted waters as measured by Hutchins and Bruland (1998), Franck et al. (2000), and Timmermans et al. (2004). This form of $R^{\text{Si:P}}$ may be thought of as generalizing the form $R^{\text{Si:P}} \propto 1/\chi_{\text{Fe}}$ employed by Matsumoto et al. (2008, 2013, 2014).

The hyperbolic iron dependence of (3) makes it difficult to control the sensitivity of $R^{\text{Si:P}}$ to increasing χ_{Fe} . In order to have direct control over this sensitivity, we consider an exponential dependence on χ_{Fe} so that the sensitivity is simply set by the e -folding DFe concentration, denoted here by χ_0 :

$$R^{\text{Si:P}} = \max \left(R_{\text{max}}^{\text{Si}} \frac{\chi_{\text{Si}}}{\chi_{\text{Si}} + k_{\text{Si:P}}^{\text{Si}}} \exp \left(-\frac{\chi_{\text{Fe}}}{\chi_0} \right), R_{\text{min}}^{\text{Si}} \right). \quad (4)$$

We do not advocate that there is any fundamental reason why the DFe dependence of $R^{\text{Si:P}}$ should be exponential, but with the parameter choices discussed below, the functional form (4) does capture the key features of the existing field data (Franck et al., 2000; Hutchins & Bruland, 1998; Timmermans et al., 2004)—see Appendix B for a comparison of observed and modeled Si:N uptake ratios. Note that the max function in (4) prevents the exponential from dropping below $R_{\text{min}}^{\text{Si}}$ with increasing DFe in order to capture $R^{\text{Si:P}}$ leveling off to a minimum value as seen in the field data.

While both exponential and hyperbolic DFe dependencies could in principle be fit to the available data, we did not perform such fits because this data has far too much scatter to narrow down a specific functional form. Instead, we use the exponential dependence here for its analytic convenience and select the value of χ_0 based on simple theoretical considerations discussed next. Other key parameters are then determined through objective optimization against the observed global nutrient climatology.

3.1. Competition Between Fertilized Diatom Growth and Decreased Si Requirement

Strengthened silicic acid leakage requires decreased silicic acid uptake U^{Si} so that more silicic acid remains in Southern Ocean surface waters from where it leaks out with mode and intermediate waters. In our model, U^{Si} is proportional to the diatom growth rate, $U_{\text{dia}}^{\text{P}}$, as expressed by (2). Because iron fertilization will increase $U_{\text{dia}}^{\text{P}}$ while decreasing $R^{\text{Si:P}}$, $R^{\text{Si:P}}$ must drop more than $U_{\text{dia}}^{\text{P}}$ increases for there to be an overall decrease in U^{Si} . For small perturbations, we have to first order

$$\frac{\delta U^{\text{Si}}}{U^{\text{Si}}} = \frac{\delta R^{\text{Si:P}}}{R^{\text{Si:P}}} + \frac{\delta U_{\text{dia}}^{\text{P}}}{U_{\text{dia}}^{\text{P}}}, \quad (5)$$

so that the fractional decrease in $R^{\text{Si:P}}$ must overcome the fractional increase in $U_{\text{dia}}^{\text{P}}$ for leakage ($\delta U^{\text{Si}} < 0$) to occur.

For our specific forms of $R^{\text{Si:P}}$ and $U_{\text{dia}}^{\text{P}}$, we can explicitly evaluate (5). For parameterization (4), for which $R^{\text{Si:P}}$ decreases exponentially with increasing DFe with e -folding concentration χ_0 , we obtain

$$\frac{\delta U^{\text{Si}}}{U^{\text{Si}}} \simeq \left(-\frac{\chi_{\text{Fe}}}{\chi_0} + \frac{2k_{\text{Fe}}}{\chi_{\text{Fe}} + k_{\text{Fe}}} \right) \frac{\delta \chi_{\text{Fe}}}{\chi_{\text{Fe}}}, \quad (6)$$

which holds where χ_{Fe} is low enough so $R^{\text{Si:P}}$ exceeds its prescribed minimum and for macronutrient-replete conditions. (The $\delta \chi_{\text{Si}}/\chi_{\text{Si}}$ and $\delta \chi_{\text{P}}/\chi_{\text{P}}$ contributions to $\delta U^{\text{Si}}/U^{\text{Si}}$ have been omitted in (6) because they are negligible in the Southern Ocean where the macronutrient concentrations far exceed the corresponding

Table 1
Key Biogeochemical Parameters of This Study

Parameter	EXP1	EXP2	HYPR	Units
χ_0	0.1 ^a	0.2 ^a	—	nM Fe
$k_{\text{Si:P}}^{\text{Fe}}$	—	—	0.077	nM Fe
$R_{\text{min}}^{\text{Si}}$	1.4 ^a	1.4 ^a	1.2	(mol Si)/(mol N)
$R_{\text{max}}^{\text{Si}}$	37.	18.	19.	(mol Si)/(mol N)
$k_{\text{Si:P}}^{\text{Si}}$	3.5	3.3	4.0	$\mu\text{M Si}$
τ_{dia}	0.65	0.69	0.65	days
τ_{nano}	1.9	1.8	1.5	days
τ_{pico}	7.8	7.7	7.4	days

Note. The values of $R_{\text{min}}^{\text{Si}}$ and $R_{\text{max}}^{\text{Si}}$ are expressed as Si:N ratios assuming a uniform uptake ratio N:P = 11:1 for diatoms (Quigg et al., 2003; Weber & Deutsch, 2010). The model's other parameters are common to the EXP1, EXP2, and HYPR cases and have the values reported by Pasquier and Holzer (2017).

^aValues were set by hand (not optimized).

half-saturation constants.) Thus, for leakage ($\delta U^{\text{Si}} < 0$) to occur in response to $\delta \chi_{\text{Fe}} > 0$, the DFe e -folding scale χ_0 of $R^{\text{Si:P}}$ needs to be sufficiently small:

$$\chi_0 \lesssim \frac{\chi_{\text{Fe}}}{2} \left(1 + \frac{\chi_{\text{Fe}}}{k_{\text{Fe}}} \right). \quad (7)$$

Note that for severe iron limitation, $\chi_{\text{Fe}} \ll k_{\text{Fe}}$, this approximates to $\chi_0 \lesssim \frac{\chi_{\text{Fe}}}{2}$. A similar analysis for the hyperbolic form 3 shows that $\delta U^{\text{Si}} > 0$ (no leakage) for small increases in χ_{Fe} . While the simple first-order analysis above cannot predict the finite-amplitude response of the highly nonlinear coupled nutrient cycles, (7) sets a useful scale for the value of χ_0 necessary for small DFe additions to enhance silicic acid leakage.

3.2. Si:P Parameter Choices, Optimization, and Fidelity to Climatology

Our parameterizations of $R^{\text{Si:P}}$ have four adjustable parameters, which cannot all be meaningfully optimized by minimizing the nutrient and phytoplankton fields against observations (attempting to do so tends to erase all dependence of the Si:P ratio on the DFe concentration). Here we consider three cases. The first is the hyperbolic iron dependence (3) for which we use the same parameters as reported by Pasquier and Holzer (2017). The other two cases use the exponential parameterization (4), for which the e -folding scale χ_0 and the minimum Si:P ratio $R_{\text{min}}^{\text{Si}}$ were fixed by hand and the other parameters ($k_{\text{Si:P}}^{\text{Si}}$ and $R_{\text{max}}^{\text{Si}}$) were jointly optimized with the three uptake timescales τ_{dia} , τ_{nano} , and τ_{pico} . All other model parameters are identical for the three cases and take the values reported by Pasquier and Holzer (2017) in their Tables 1 and 2.

Our choices for χ_0 are based on (7). For the unperturbed iron cycle, our model produces a SO DFe concentration of $\chi_{\text{Fe}} \sim 0.15$ – 0.16 nM for all Si:P parameterizations considered. With the model's iron half-saturation constant for diatom growth of $k_{\text{Fe}} = 0.30$ nM (Pasquier & Holzer, 2017), this means we expect leakage for $\chi_0 \lesssim 0.12$ nM. We therefore consider $\chi_0 = 0.1$ nM, which should produce leakage for even small iron additions to the Southern Ocean. To address the question if a less sensitive Si:P dependence can produce leakage for a finite-amplitude perturbation (for which the linear analysis that led to (7) does not apply), we also consider $\chi_0 = 0.2$ nM. The minimum Si:P uptake ratio, $R_{\text{min}}^{\text{Si}}$, was chosen so that the optimization yielded reasonable values for the other parameters. The value of $R_{\text{min}}^{\text{Si}} = 1.4$, in terms of Si:N, is higher than the iron-replete value of Si:N = 1:1 often cited in modeling studies (e.g., Matsumoto et al., 2002), but lies well within the observed variability across different species and environmental parameters (see also Appendix B, Figure B1; Brzezinski, 1985).

We will refer to the three Si:P parameterizations considered as EXP1, EXP2, and HYPR, for exponential DFe dependence with $\chi_0 = 0.1$ nM, exponential with $\chi_0 = 0.2$ nM, and hyperbolic DFe dependence, respectively. The values of the $R^{\text{Si:P}}$ parameters and the optimized uptake timescales are collected in Table 1. As shown in Appendix B, all three parameterizations are broadly consistent with the available laboratory and field data

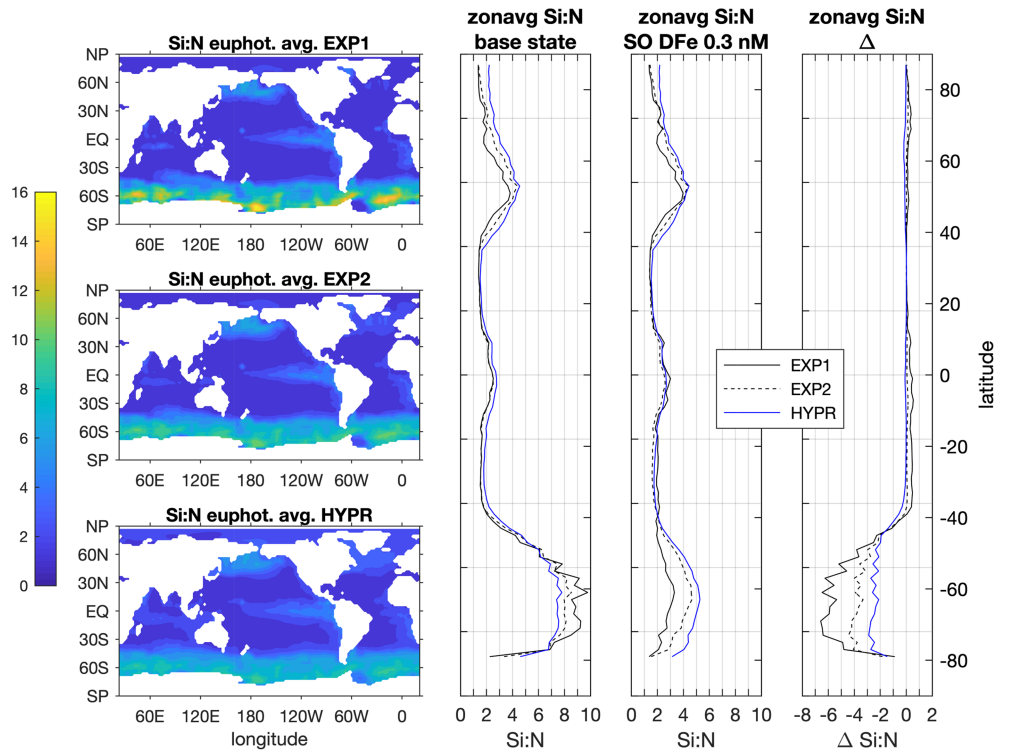


Figure 1. Maps of the Si:P uptake ratio (expressed as Si:N using N:P = 11:1 for diatoms) of the unperturbed base state averaged vertically over the euphotic zone and its zonal average for the three Si:P cases considered (EXP1, EXP2, and HYPR). Also shown are the zonal averages for the fertilized state corresponding to a doubling of SO DFe to 0.3 nM and the anomalies from the base state.

for the Si:N uptake ratio, but EXP1 could be argued to come closest to capturing the field data at the lowest measured DFe concentrations ($\lesssim 0.3$ nM).

Figure 1 shows maps and zonal averages of our three parameterizations of the Si:P uptake ratio, averaged vertically over the euphotic zone and expressed as Si:N assuming a constant N:P = 11:1 for diatoms (Quigg et al., 2003; Weber & Deutsch, 2010). In the unperturbed base states, all three cases have similar Si:P patterns, with zonal averages that differ by only $\sim 10\%$ among the three cases, although large Si:P uptake ratios near Antarctica are higher for the EXP1 case than for the other two. Note that Si:N values of nearly 16 visible in small Southern Ocean patches for EXP1 are still within the observed range for low DFe (Appendix B). The unperturbed zonal-mean Si:P uptake ratios are consistent with the observation-based estimates of the ratio of Si uptake to total P uptake (all plankton, not just diatoms, and thus a lower bound) diagnosed by Roshan et al. (2018) using a diagnostic inverse model.

The zonal-mean Si:P uptake ratio at a fertilization amplitude with SO DFe = 0.3 nM and its anomaly from the unperturbed base state are also shown in Figure 1. The three Si:P cases respond very differently to Southern Ocean iron fertilization. By construction, both EXP1 and EXP2 decrease their Si:P uptake ratio more than the HYPR case, with EXP1 having the strongest decreases. At this level of fertilization, the EXP1 Si:P uptake ratio approaches that of the ambient water (not shown), but as discussed in section 3.1 this is not necessary for enhanced Si leakage, which for EXP1 already occurs for much smaller perturbations.

All three optimized cases (EXP1, EXP2, HYPR) allow us to fit the nutrient climatology with nearly the same fidelity, which for the HYPR case was documented in detail by Pasquier and Holzer (2017). For all cases, the global root-mean-square (RMS) errors for the volume-weighted mismatch are 5.1%, 12%, and 44% of the global mean concentrations for PO_4 , $\text{Si}(\text{OH})_4$, and DFe, respectively. Importantly, the optimized unfertilized base states of the three Si:P parameterizations have nearly identical nutrient cycles both in terms of the three-dimensional nutrient distributions and in terms of quantitative cycling metrics, discussed further below. Employing nearly identical base states embedded in the same ocean circulation ensures that

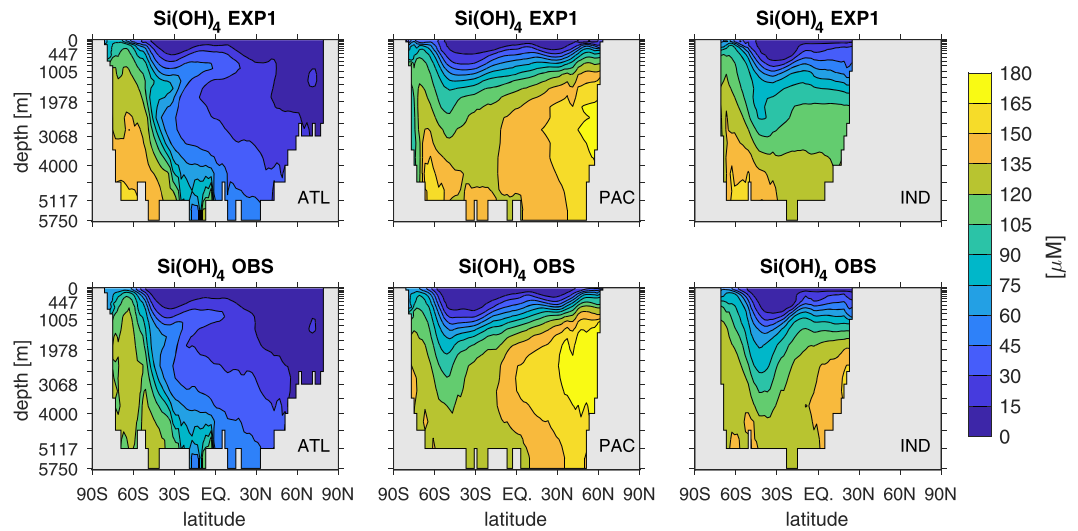


Figure 2. Basin zonal averages of the silicic acid concentration for the EXP1 case compared to the observational climatology from WOA13 against which the inverse model was optimized. The comparisons for the EXP2 and HYPR cases (not shown) are nearly identical.

differing responses to iron fertilization can be ascribed to differences in the parameterization of the Si:P uptake ratio.

The basin zonal averages of $\text{Si}(\text{OH})_4$ are shown for the EXP1 case in Figure 2 together with the corresponding observational fields. The observed patterns are overall well matched, but biases are also visible: An overestimate of the $\text{Si}(\text{OH})_4$ concentration in the intermediate, mode, and bottom waters of the Southern Hemisphere and an underestimate in the North Pacific, northern Indian Ocean, and deep North Atlantic. Similar biases for $\text{Si}(\text{OH})_4$, in both pattern and magnitude, occur when silicic acid utilization is modeled by conditionally restoring surface concentrations to observations (Holzer et al., 2014; Holzer & Brzezinski, 2015). These biases may be due to the very simple parameterization of opal dissolution or to residual biases in the data-assimilated circulation (Primeau et al., 2013).

4. Results

4.1. Nutrient Response to Iron Fertilization

Before considering systematic variations with fertilization amplitude, we first consider the spatial structure of the nutrient concentration anomalies for $\text{SO DFe} = 0.3 \text{ nM}$. Figure 3 shows the basin zonal averages of the silicic acid anomaly from the unperturbed state. The effect of the different Si:P parameterizations is immediately evident: The HYPR case shows no enhanced leakage—instead silicic acid is trapped more strongly in the Southern Ocean and the $\text{Si}(\text{OH})_4$ concentrations in the upper ocean are reduced from their unperturbed values. For the HYPR case, increased biological diatom production (quantified separately below) wins over reduced Si:P uptake ratio and Southern Ocean $\text{Si}(\text{OH})_4$ utilization increases. As a result, lower $\text{Si}(\text{OH})_4$ concentrations exit the Southern Ocean with mode and intermediate waters, reducing the $\text{Si}(\text{OH})_4$ concentrations in the upper ocean.

The EXP1 case responds to a doubling of SO DFe as predicted: The reduced Si:P requirement wins over increased diatom growth. As a result, excess $\text{Si}(\text{OH})_4$ on the order of $15 \mu\text{M}$ exits the Southern Ocean in mode and intermediate waters and the upper-ocean $\text{Si}(\text{OH})_4$ concentration rises north of the Southern Ocean. Correspondingly, less silicic acid is trapped in the deep Southern Ocean. The differences between the basins reflect the differences in their circulation: In the Atlantic, NADW returns the excess silicic acid to depth in the North Atlantic, while the deep overturning cell of the Pacific and Indian Ocean carries the lower concentrations of the deep Southern Ocean northward.

The EXP2 case is intermediate at this perturbation amplitude. Enhanced diatom production decreases silicic acid in Antarctic waters, but in subantarctic waters, reduced Si:P uptake ratio wins causing weakly enhanced silicic acid leakage to the rest of the ocean. Because both enhanced Southern Ocean trapping

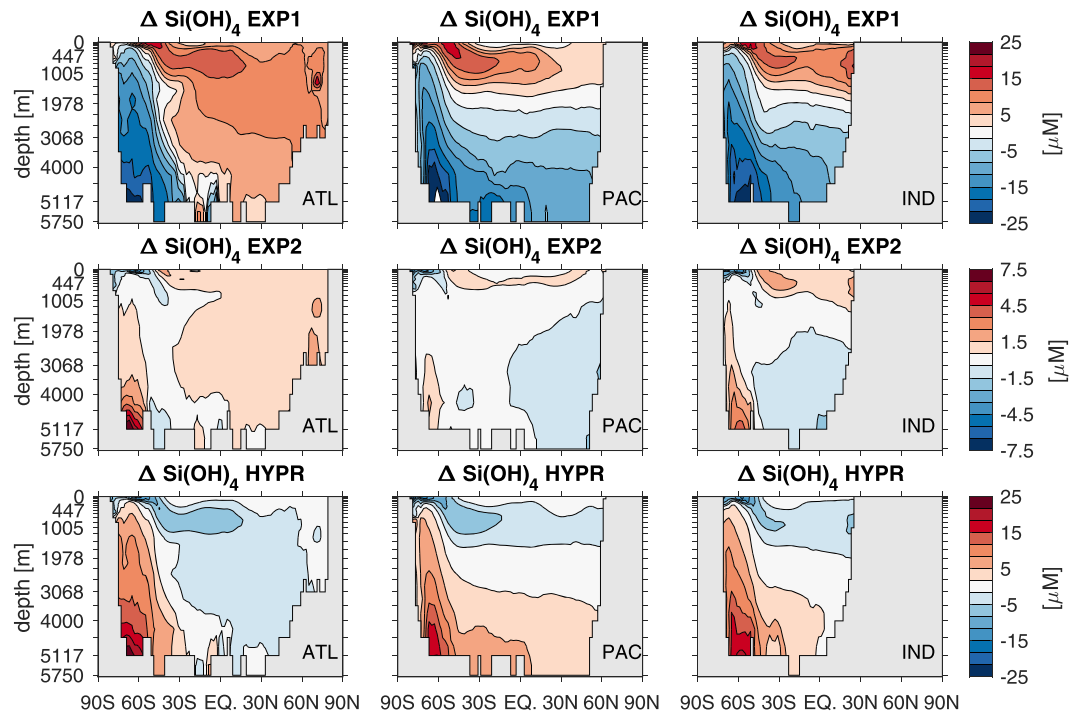


Figure 3. Anomalies in the basin zonal averages of the silicic acid concentration for all three Si:P cases (EXP1, EXP2, HYPR) at the Southern Ocean iron fertilization level corresponding to a doubling of SO DFe to 0.3 nM. Note the separate color scale for the EXP2 case.

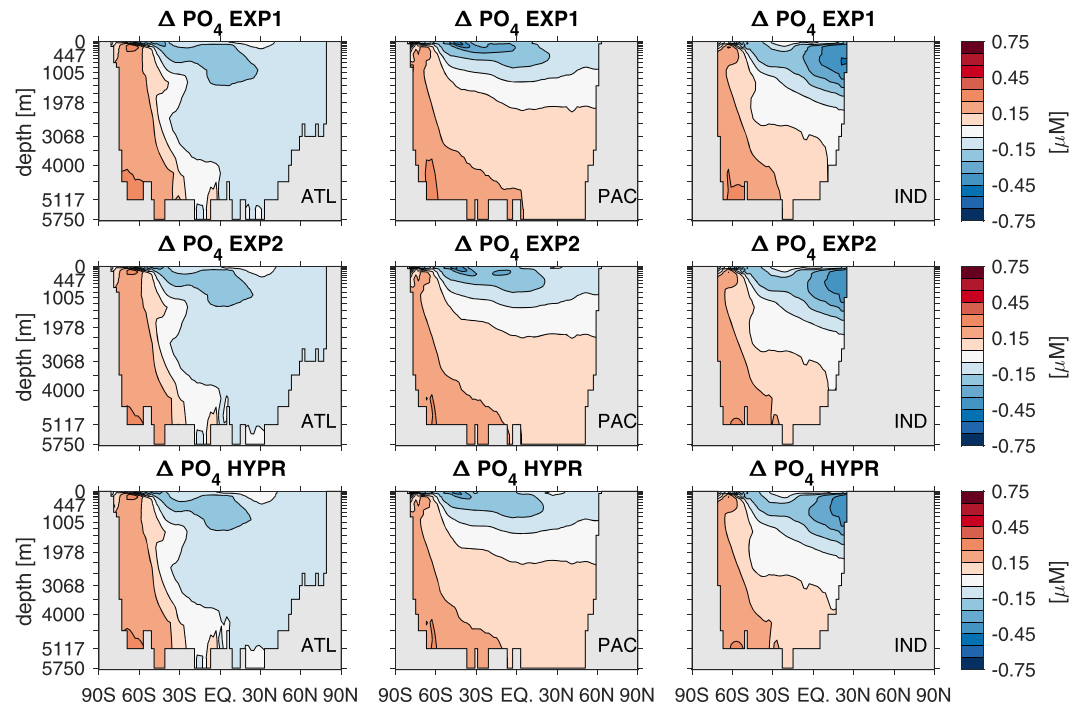


Figure 4. Anomalies in the basin zonal averages of the PO₄ concentration for all three Si:P cases at the Southern Ocean iron fertilization level corresponding to a doubling of SO DFe to 0.3 nM.

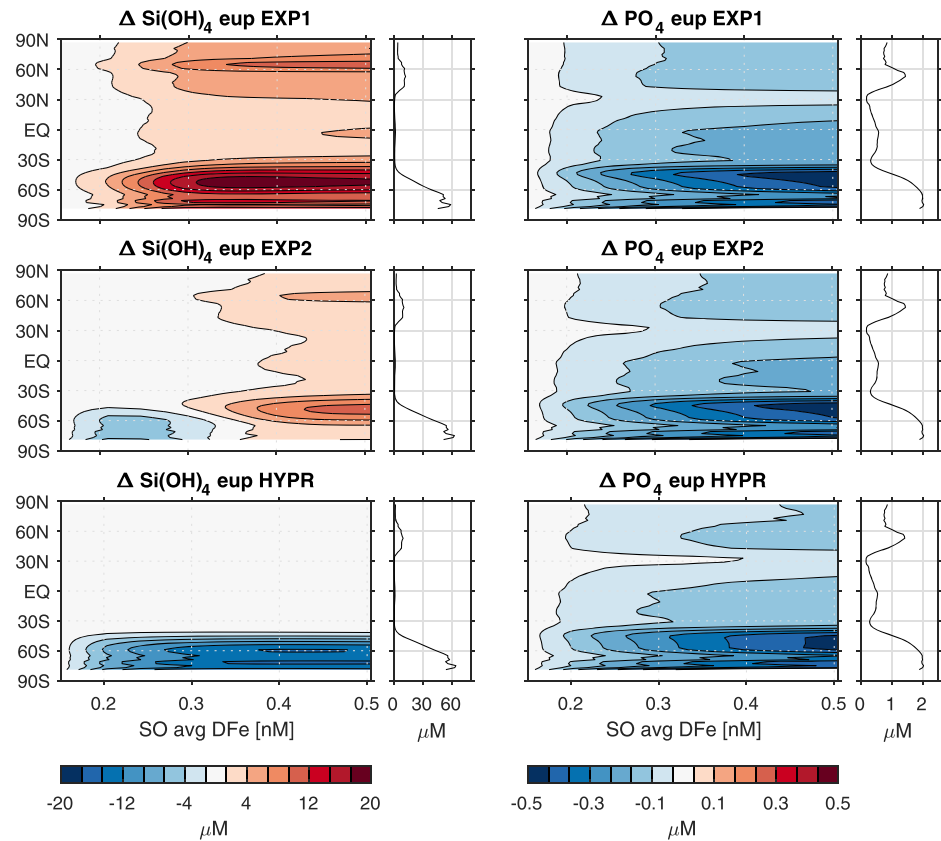


Figure 5. Anomalies in the zonally averaged euphotic-zone Si(OH)_4 (left) and PO_4 (right) concentrations as a function of SO DFe. The unperturbed base state zonal averages are shown as line plots to place the magnitude of the anomalies in context.

and subantarctic leakage occur, the overall amplitude of the Si(OH)_4 response is much weaker than for the EXP1 case.

Figure 4 shows the response of the zonally averaged PO_4 concentration. Although the phosphorus and silicon cycles are coupled, differences in the Si:P uptake ratio result in only very minor differences in the PO_4 response. For all three Si:P cases, fertilizing the Southern Ocean leads to increased vertical export of particulate organic matter, resulting in strengthened Southern Ocean phosphorus trapping and a corresponding drawdown of phosphate out of the upper ocean.

The response of the DFe field (not shown) is similarly insensitive to the form of the Si:P uptake ratio, with DFe increasing throughout the Southern Ocean water column as more DFe is added to the Southern Ocean surface. DFe is transported to depth by both the biological and scavenging pumps (Pasquier & Holzer, 2017, 2018)—see Appendix A, Figure A2 for the zonal-mean surface response.

The systematic response of macronutrients in the euphotic zone as a function of SO DFe is shown in Figure 5 in terms of global zonal-mean concentrations. We first consider silicic acid (left panels). The HYPR case shows a drawdown of silicic acid in the Southern Ocean that becomes ever more pronounced with increasing DFe, saturating for SO DFe ≥ 0.4 nM. For the HYPR case, silicic acid in the rest of the surface ocean is barely affected (confirmed by examining maps, not shown). By contrast, the EXP1 case shows increasing silicic acid concentrations at all latitudes, with the largest increases in the subpolar oceans. In the Southern Ocean, these increases saturate for SO DFe ≥ 0.35 nM DFe. Maps (not shown) reveal that the mid- and low-latitude increases of Si(OH)_4 occur primarily in the Atlantic and Indian oceans (~ 5 μM for a SO DFe doubling, and ~ 9 μM for SO DFe ~ 0.5 nM), while in the Pacific subtropical gyres Si(OH)_4 increases by less than 1.5 μM . The tropical and Northern Hemisphere increases in surface Si(OH)_4 are the result of increased Si(OH)_4 leakage from the Southern Ocean and not due to a reduced Si requirement induced by additional DFe transported from the Southern Ocean (see export discussion below). The EXP2 response is again intermediate: only

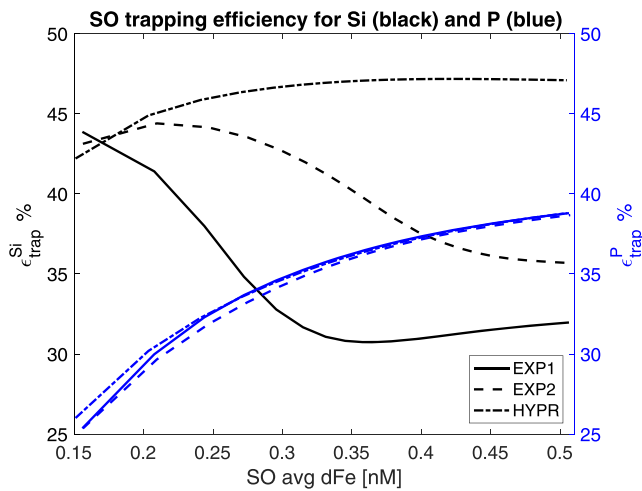


Figure 6. The efficiency with which silicic acid ($\epsilon_{\text{trap}}^{\text{Si}}$, black curves, left ordinate) and phosphate ($\epsilon_{\text{trap}}^{\text{P}}$, blue curves, right ordinate) are trapped in the Southern Ocean as a function of SO DFe for the three cases of the Si:P uptake ratio.

shows ϵ_{trap} for silicon and phosphorus as a function of iron fertilization amplitude. In the unperturbed base states, $\epsilon_{\text{trap}}^{\text{Si}} \sim 43\%$ for all three Si:P cases (black curves, left ordinate). For the more strongly trapping HYPR case, $\epsilon_{\text{trap}}^{\text{Si}}$ increases to $\sim 47\%$, while for the more strongly leaking EXP1 case, $\epsilon_{\text{trap}}^{\text{Si}}$ decreases to $\sim 32\%$ at the largest fertilization amplitude. The EXP1 case displays weak nonmonotonic behavior with a slight recovery from a minimal trapping efficiency at SO DFe ~ 0.35 nM as the nonlinear system adjusts to further increasing iron input. This recovery may possibly be due to the increase in the Si:P uptake ratio with increased surface silicic acid in regions that are still sufficiently iron limited for Si:P to depend on silicic acid concentration (i.e., for Si:P not clamped at its minimum). Even at the highest perturbation amplitude, diatoms in the subpolar North Pacific and eastern tropical Pacific remain iron limited (Appendix C and Figure C1). The dominantly iron-limited part of the eastern tropical Pacific shrinks as the equatorial Pacific becomes iron-phosphate colimited consistent with strengthened Southern Ocean PO_4 trapping and limited DFe increases outside of the Southern Ocean (Figure A2). For the EXP2 case, $\epsilon_{\text{trap}}^{\text{Si}}$ first increases but then decreases to about 36% as SO DFe increases beyond ~ 0.2 nM and silicic acid becomes increasingly untrapped.

The phosphate trapping efficiency, $\epsilon_{\text{trap}}^{\text{P}}$, is roughly 25% in the unperturbed state and then increases with iron fertilization in nearly identical fashion for all three Si:P cases (blue curves, right ordinate). As biological production in the Southern Ocean is increasingly fertilized, injection of particulate organic phosphorus into upwelling circumpolar deepwaters increases, trapping phosphorus ever more strongly in the Southern Ocean. For SO DFe ~ 0.5 nM, $\epsilon_{\text{trap}}^{\text{P}}$ reaches 39%.

4.2. Export Response to Iron Fertilization

The left panels of Figure 7 show the anomalies in the zonally integrated opal export as a function of SO DFe together with the base-state opal export. For the HYPR case, Southern Ocean iron fertilization primarily increases opal export in the Southern Ocean, but there is also a small poleward shift resulting in a dipolar export anomaly. The resulting increased Southern Ocean silicon trapping causes a reduction in tropical opal export. By contrast, the EXP1 case exhibits strongly reduced Southern Ocean opal export with no poleward shift as the perturbation amplitude increases. The resulting enhanced leakage of silicic acid to the rest of the ocean drives a smaller increase in opal export at low latitudes that occurs primarily in the tropical eastern Pacific and in the eastern South Atlantic ($0\text{--}30^\circ\text{S}$, map not shown). The Southern Ocean opal export anomaly approximately saturates for SO DFe ≥ 0.35 nM, with a peak reduction in the Southern Ocean of $\sim 42\%$ at 55°S , and a peak enhancement of $\sim 27\%$ at the equator. The EXP2 case is intermediate, displaying the characteristics of the HYPR case for SO DFe ≤ 0.3 nM and of the EXP1 case for larger SO DFe.

The right panels of Figure 7 show the zonally integrated phosphorus export converted to carbon units using C:P = 106:1. (This is not meant to be a precise estimate of carbon export as the C:P export ratio is known to

for SO DFe ≥ 0.3 nM does the Southern Ocean start to leak with a response that is similar to the EXP1 case at lower fertilization levels. At small fertilization amplitudes, the EXP2 case is dominated by increased Southern Ocean diatom production and $\text{Si}(\text{OH})_4$ drawdown.

The surface PO_4 response (Figure 5, right panels) is broadly similar for all three Si:P cases: Southern Ocean iron fertilization increases PO_4 drawdown and trapping in the Southern Ocean. As more PO_4 is drawn into the Southern Ocean, the surface PO_4 concentration drops globally, with the smallest response in the subtropical gyres where the base state has already low PO_4 concentrations (~ 0.2 μM in the zonal mean). Maps (not shown) reveal that the largest reductions north of the Southern Ocean occur in the eastern tropical and eastern South Pacific, where the upwelling supply of PO_4 is suppressed by increased Southern Ocean trapping.

4.1.1. Southern Ocean Nutrient Trapping

We quantify Southern Ocean nutrient trapping in terms of the trapping efficiency ϵ_{trap} , defined as the fraction of the global nutrient inventory that was last utilized south of 38°S and that will next be utilized south of 38°S (Holzer et al., 2014). In other words, ϵ_{trap} is the fraction of the global nutrient inventory in transit between successive biological utilizations south of 38°S . (Note that Holzer et al. (2014) denote the same quantity by R_{trap} ; here we use ϵ_{trap} to avoid confusion with stoichiometric ratios.) Figure 6

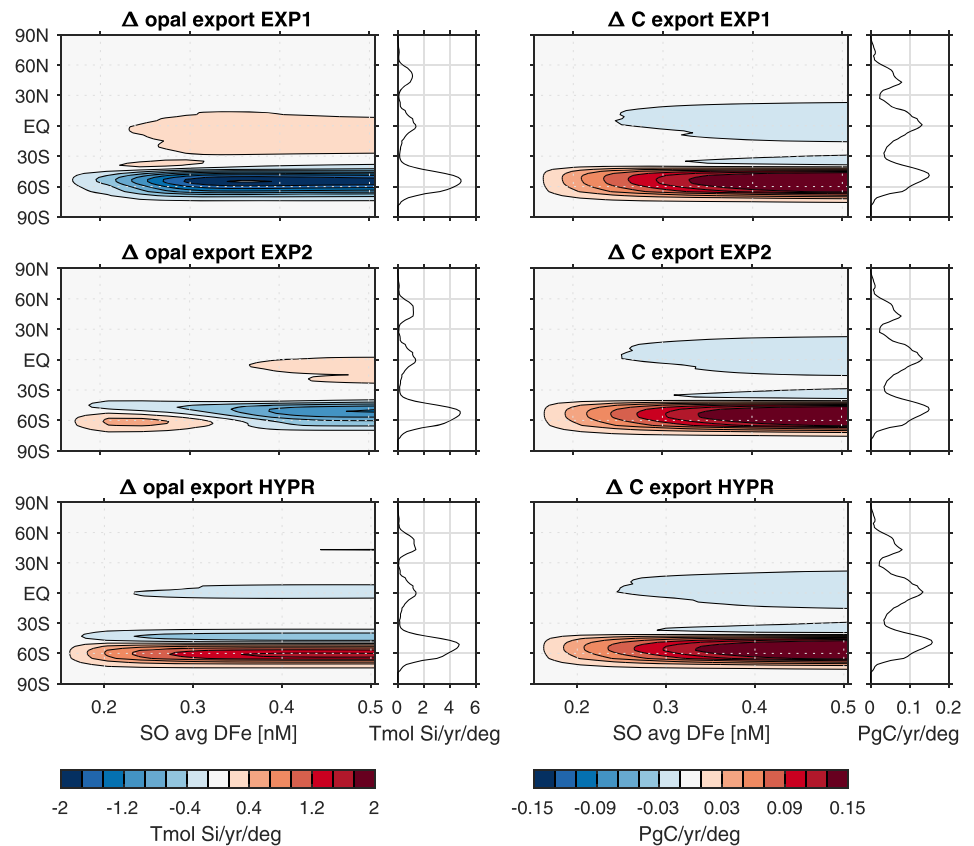


Figure 7. Anomalies in the zonally integrated exports of Si (left) and P (right) as a function of SO DFe. The P export has been expressed in carbon units using a constant C:P = 106:1. The unperturbed base-state zonal averages are shown as line plots to place the magnitude of the anomalies in context.

vary with phosphate concentration, Galbraith & Martiny, 2015, but merely a unit conversion for the reader more familiar with export magnitudes in carbon units.) The anomalous phosphorus exports are remarkably similar for all three Si:P cases. There is a strong enhancement in the Southern Ocean reflecting the fertilized production. There are weaker decreases near the equator reflecting the reduced low-latitude PO_4 supply due to increased Southern Ocean phosphorus trapping. The phosphorus export anomalies show no sign of saturation with increasing iron fertilization likely because even at the highest fertilization amplitude the Monod limitation terms have not yet saturated for PO_4 and DFe. The peak anomalies at the highest fertilization level represent about a 150% increase in the Southern Ocean and a 17% decrease in the tropics.

The globally integrated opal and phosphate exports (the latter again expressed in carbon units) are plotted as a function of SO DFe in Figure 8a. The global phosphorus export (blue, right ordinate) increases for all Si:P cases from ~ 10 Pg C/yr for the base state to ~ 13.5 Pg C/yr for the largest perturbation. The global opal export (black, left ordinate) of the base states is ~ 170 Tmol Si/yr for all three Si:P cases, but the responses to iron fertilization depend strongly on the $R^{\text{Si:P}}$ parameterization. For the more strongly leaking EXP1 case, the global opal export decreases to about 142 Tmol Si/yr for SO DFe ~ 0.35 nM and approximately levels off around this value for larger perturbations. For the more strongly trapping HYPR case, the global opal export increases monotonically with increasing SO DFe and levels off around 182 Tmol Si/yr for SO DFe ≥ 0.35 nM. For the intermediate EXP2 case, the global opal export rises by a few Tmol Si/yr until SO DFe increases beyond ~ 0.2 nM, after which the opal export falls to ~ 156 Tmol Si/yr at the largest fertilization amplitude.

Figure 8b quantifies the role of diatoms in organic matter export, which becomes increasingly important as iron fertilization lowers the Si:P uptake ratio. The base-state fraction of phosphorus export due to diatoms ranges from 41% to 47% for the different Si:P cases, consistent with other modeling studies (e.g., Aumont et al., 2003; Moore et al., 2004) and observation-based estimates (Nelson et al., 1995). For all cases, the fraction of the phosphorus export by diatoms increases monotonically with increasing SO DFe. At the largest

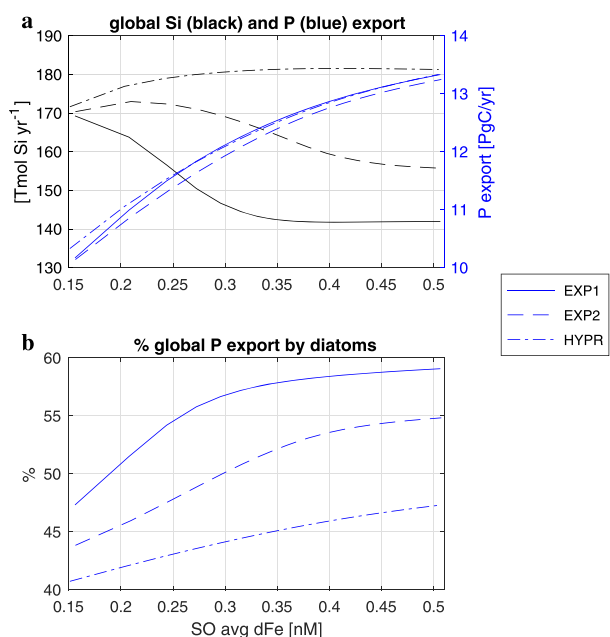


Figure 8. (a) The globally integrated opal and organic phosphorus exports (converted to carbon units with C:P = 106:1), and (b) the percentage of the global phosphorus export due to diatoms. Note that for (a) the ordinate for opal export (black curves) is on the left, and the ordinate for phosphorus export (blue curves) is on the right.

perturbation amplitude, this fraction reaches 59% for EXP1, 55% for EXP2, and 47% for HYPR. We examine the response of the diatom biomass in more detail in the next section.

For all Si:P cases, the fraction of the global phosphorus export due to diatoms is dominated by the Southern Ocean response. Indeed, for the EXP1 and EXP2 cases at the largest fertilization amplitude, the anomaly in the fraction of the global phosphorus export due to diatoms south of 40°S is about 1.5 times larger than the anomaly of the global fraction. For EXP1 and EXP2, the phosphorus export by diatoms north of 40°S increases slightly with iron fertilization (see below), but the global phosphorus export increases much more, driven mostly by increases in the Southern Ocean. Thus, the anomaly in the fraction of the global export from diatoms north of 40°S actually decreases by a few percent with iron fertilization. For the HYPR case, this effect is even stronger (the factor of 1.5 becomes 2.0) because in this case the absolute phosphorus export by diatoms decreases outside of the Southern Ocean.

Increasing carbon export with iron fertilization implies an increased efficiency of the biological pump. We quantify the pump efficiency $E_{\text{bio}}^{\text{P}}$ following Ito and Follows (2005) as the ratio of regenerated to total phosphate inventory, and we similarly define a biological silicon pump efficiency $E_{\text{bio}}^{\text{Si}}$ as the ratio of the regenerated to total silicic acid inventory. These efficiencies (not shown) display virtually the same systematic behavior as the global exports. For all Si:P cases, the unperturbed base states are characterized by $E_{\text{bio}}^{\text{P}} \sim 43\%$ and $E_{\text{bio}}^{\text{Si}} \sim 66\%$. At the largest fertilization amplitude, $E_{\text{bio}}^{\text{P}}$ increases to 52% for all Si:P cases, while $E_{\text{bio}}^{\text{Si}}$ drops to around 55% for the leaking EXP1 case and rises to nearly 72% for the trapping HYPR case.

4.3. Changes in the Role of Diatoms

Here we examine the effects of Southern Ocean iron fertilization on phytoplankton community structure and the role of diatoms in organic matter export. As shown by Pasquier and Holzer (2017), in the unperturbed base state diatoms are silicon colimited with phosphate and/or iron in the subtropical gyres and iron limited at high latitudes and in the eastern tropical Pacific, consistent with the available field data (Moore et al., 2013). For reference, the diatom nutrient limitation patterns are defined and plotted in Appendix C for both the unperturbed and iron-fertilized (SO DFe ~ 0.5 nM) states. For all phytoplankton classes and Si:P cases, iron addition to the Southern Ocean reduces iron limitation primarily in the Southern Ocean, raising the DFe Monod limitation factor there by 0.2 to 0.6 at the highest perturbation amplitude, depending on location and functional class. Increased Southern Ocean phosphate trapping lowers the phosphate nutrient limitation everywhere, thus increasing phosphate deficiency with P Monod terms dropping by as much as 0.4 at the poleward edge of the South Pacific subtropical gyre.

Silicic acid leakage (EXP1, EXP2) at the highest fertilization amplitude nearly eliminates silicic acid colimitation in the Atlantic (Si Monod factors in excess of 0.8 except for a small region in the South Atlantic gyre, where the Si Monod factor remains as low as 0.6). However, even at the highest fertilization rate, the central Pacific subtropical gyres remain silicon colimited with the Monod factors of all three nutrients ($\text{Si}(\text{OH})_4$, PO_4 , and DFe) remaining below 0.5. Si-P-Fe colimitation in the equatorial Pacific is replaced by Fe-P colimitation, except in the eastern upwelling region where Fe limitation persists. For the HYPR case, increased Southern Ocean Si and P trapping leaves the diatom limitation patterns in the Atlantic largely unchanged, a region of Fe-Si colimitation in the tropical eastern Pacific becomes also P colimited, and the Indian Ocean becomes mostly P limited. In our model, phytoplankton concentration is proportional to their specific growth rate, which is proportional to the product of Monod terms, so that changes in nutrient limitation will manifest themselves in changes of the phytoplankton community structure.

Figure 9 shows maps of the percentage of the phytoplankton biomass that is diatoms in the base state, in the perturbed state corresponding to a doubling of SO DFe, and the corresponding anomaly. The base-state fractional diatom abundance is nearly identical for all three Si:P cases, with $\sim 30\%$ diatoms at high latitudes.

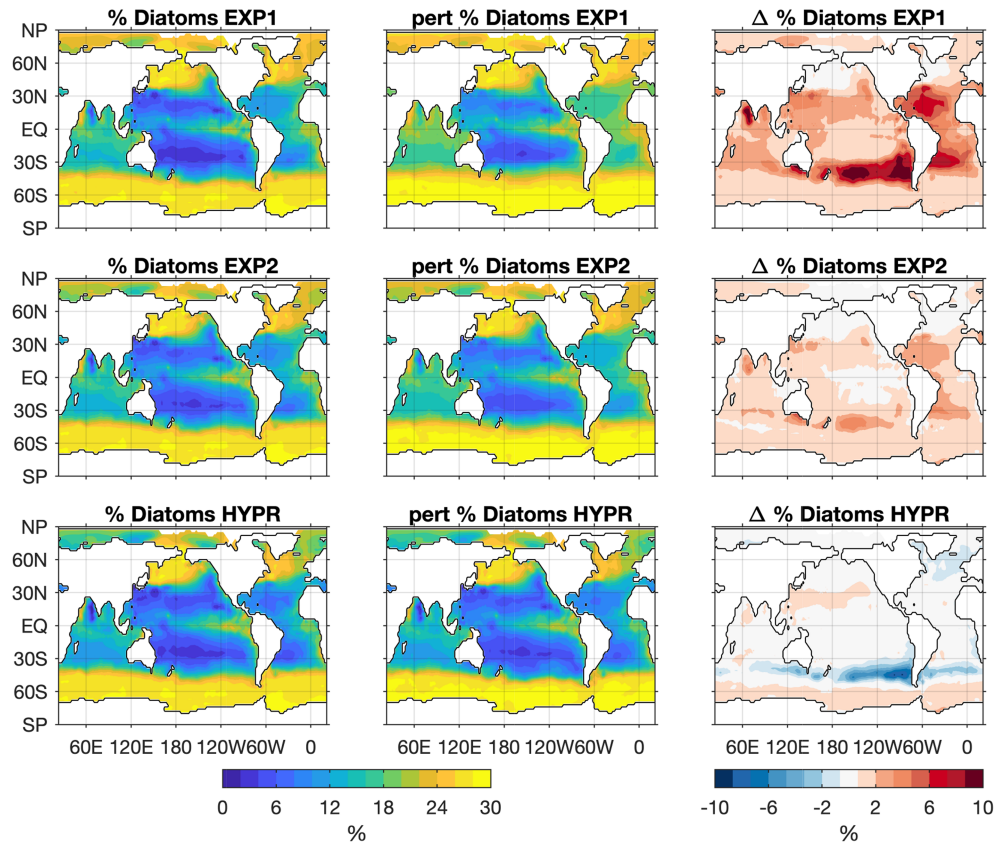


Figure 9. Geographic distribution of the diatom percentage of the phytoplankton biomass. Shown are the unperturbed base states (left), the perturbed states corresponding to a doubling of SO DFe (middle), and the corresponding anomalies (right).

The response to iron fertilization depends strongly on the details of the Si:P uptake ratio. For the HYPR case, the dominant effect is a contraction of the Southern Ocean diatom belt toward the Southern Ocean, with the largest anomaly being a drop of 5–9% in the absolute diatom fraction in the midlatitude South Pacific immediately north of the fertilized region. For the EXP1 case, the diatom percentage increases everywhere, the dominant effect being an expansion into the subtropical gyres especially in the Atlantic and in the midlatitude South Pacific where the absolute local diatom fraction increases by ~10%. (Note that these are absolute changes, not relative changes; for example if the unperturbed diatom fraction is 5%, an absolute increase by 10% means a change to 15%.) At this level of fertilization, the EXP2 case has a similar response pattern as EXP1 but of smaller amplitude. With increasing fertilization, the EXP1 pattern changes little while the EXP2 pattern intensifies to become more like EXP1.

For the EXP1 and EXP2 cases with enhanced silicic acid leakage, a more detailed analysis shows that increases in the low-latitude diatom fraction in the Pacific are dominated by increases in the diatom biomass, while increases in the Atlantic diatom fraction are due to both diatom increases and nondiatom decreases, with similar contributions. In the Indian Ocean (other than the Arabian Sea), increases in the diatom fraction occur in spite of slight decreases in diatom biomass because of much larger decreases in the nondiatom biomass. In the Arabian Sea, the diatom biomass increases, while nondiatoms decrease. Increases in the diatom concentration are driven by enhanced silicic acid leakage, while decreases in the concentration of the other phytoplankton classes are driven by decreased surface phosphate.

The response of the absolute diatom biomass is completely dominated by the Southern Ocean where diatoms increase by about 4 mg C/m^3 at the highest fertilization rate for all three Si:P cases. The systematic behavior as a function of fertilization amplitude is summarized in Figure 10 (right panels) in terms of the zonally and vertically integrated diatom biomass. Peak increases at the highest fertilization rate are ~60% at about 57°S . The Southern Ocean response dwarfs the low-latitude response, which is about an order of magnitude

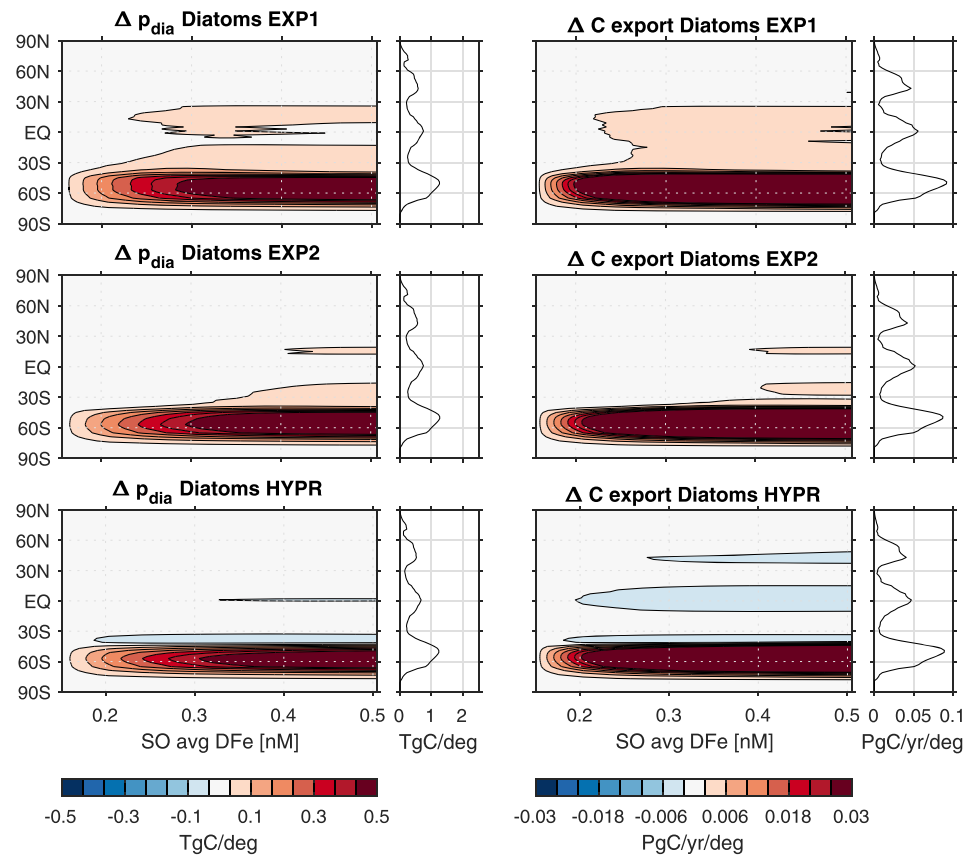


Figure 10. Anomalies in the zonally and vertically integrated diatom concentration p_{dia} (left) and zonally integrated diatom phosphorus export (right), both converted to carbon units, as a function of SO DFe. The unperturbed base-state zonal averages are shown as line plots to place the magnitude of the anomalies in context.

smaller. Because uptake is proportional to phytoplankton concentration, and export is proportional (with a detrital fraction that depends only on temperature) to uptake, the anomalies in carbon export due to diatoms (Figure 10, left panels) approximately mirror the biomass anomalies.

The low-latitude response to enhanced silicic acid leakage (EXP1 and EXP2) is limited by increased phosphate limitation due to stronger Southern Ocean phosphorus trapping and by persistent iron limitation in the tropical Pacific, which is not alleviated by Southern Ocean fertilization (Appendices A and C). Thus, while the floristic shifts occur mostly at low latitudes, they correspond to only small absolute changes in diatom biomass and diatom carbon export. In the Southern Ocean, diatom and nondiatom phytoplankton respond strongly to iron fertilization but in roughly equal proportions, which leads to large increases in absolute diatom mass and export but only to small changes in the diatom fraction. Nondiatom phytoplankton (not shown) responds with enhanced Southern Ocean biomass and export but decreased biomass and export outside the Southern Ocean. The low-latitude decreases are most pronounced for the EXP1 case and least pronounced for the HYPR case, reflecting competition with diatoms when there is enhanced silicic acid leakage from the Southern Ocean.

4.4. Isotope Signature of the Response

Key information about past states of the ocean's silicon cycle comes from the $\delta^{30}\text{Si}$ isotope signature of biogenic opal in the sediments (e.g., Beucher et al., 2007; Brzezinski et al., 2002). Here we examine how the iron dependence of the Si:P uptake ratio and the strength of Southern Ocean iron fertilization imprint on the $\delta^{30}\text{Si}$ signature of opal flux in the modern ocean circulation.

To compute $\delta^{30}\text{Si}$, we follow the approach of Holzer and Brzezinski (2015), and we assume that fractionation on dissolution is negligible. (The adjustable parameter of δ_{avg} in that approach, which sets the global mean isotope ratio, was objectively optimized to a value of $\delta_{\text{avg}} = +1.27\%$, slightly lower than the value of

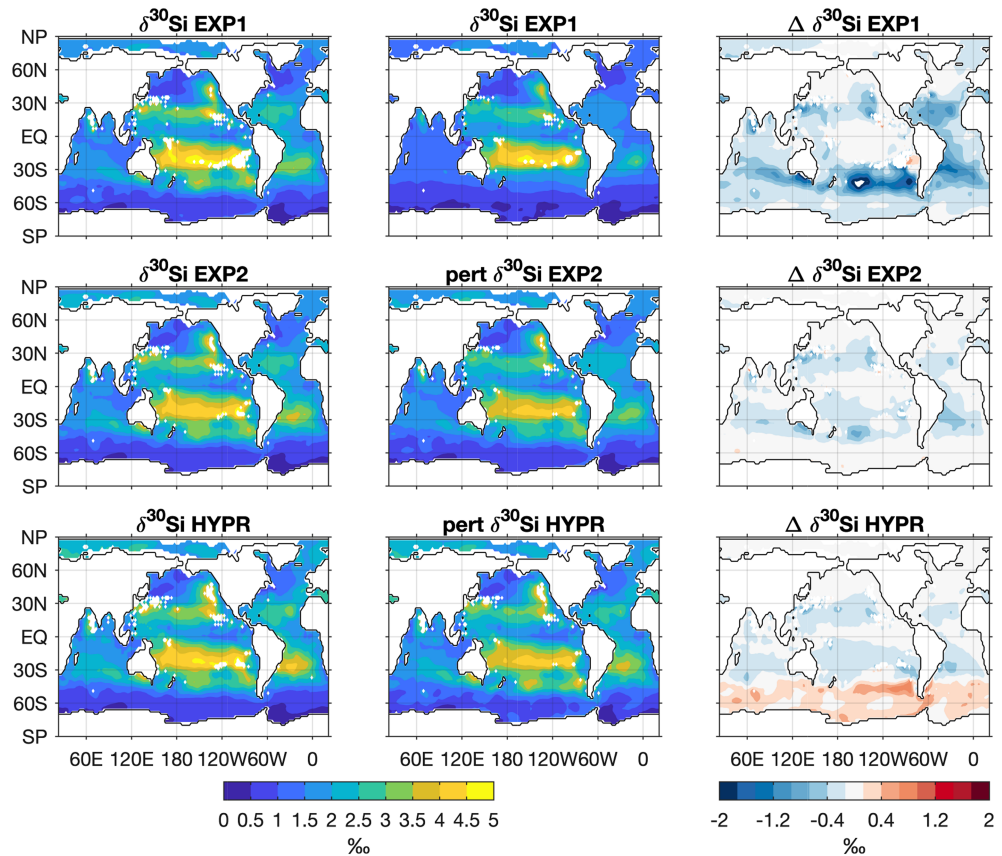


Figure 11. $\delta^{30}\text{Si}$ of the opal flux onto the sediments. Shown are the unperturbed base states (left), the perturbed states corresponding to a doubling of SO DFe (middle), and the corresponding anomalies (right).

+1.29‰ used by Holzer & Brzezinski, 2015.) Below we examine the $\delta^{30}\text{Si}$ value of the opal flux onto the sediments, denoted as $\delta^{30}\text{Si}_{\text{sed}}$. In accord with basic isotope dynamics (e.g., Beucher et al., 2007), $\delta^{30}\text{Si}_{\text{sed}}$ is to computational accuracy given by the $\delta^{30}\text{Si}_{\text{eup}}$ value of $\text{Si}(\text{OH})_4$ in the overlying euphotic zone shifted by the fractionation factor, that is, $\delta^{30}\text{Si}_{\text{sed}} = \delta^{30}\text{Si}_{\text{eup}} - 1.1\text{‰}$, so that the euphotic and sediment $\delta^{30}\text{Si}$ values have the same anomalies.

Figure 11 shows maps of the base-state $\delta^{30}\text{Si}_{\text{sed}}$, the perturbed $\delta^{30}\text{Si}_{\text{sed}}$ for a doubling of SO DFe, and the corresponding anomalies. All Si:P parameterizations show roughly the same base state $\delta^{30}\text{Si}_{\text{sed}}$ distribution but when iron is added to the Southern Ocean, the sediment isotope response is very different for the different Si:P parameterizations. The pattern of $\delta^{30}\text{Si}_{\text{sed}}$ is roughly anticorrelated with the pattern of the fractional change in the euphotic $\text{Si}(\text{OH})_4$ concentration, which plays a role in shaping the fractional diatom abundance through the Si Monod factor of diatom growth (see Figure 9). The fertilized HYPR case with its increased Southern Ocean silicon trapping produces isotopically heavier opal flux in the Southern Ocean, while the EXP1 case with its increased silicic acid leakage shows isotopically lighter opal fluxes throughout, with the greatest decreases in $\delta^{30}\text{Si}_{\text{sed}}$ where the largest relative changes in euphotic-zone silicic acid occur. The EXP2 case has a similar $\delta^{30}\text{Si}_{\text{sed}}$ pattern as EXP1, but with a reduced amplitude consistent with reduced anomalies in euphotic-zone silicic acid concentration and diatom fraction.

Figure 12 shows the systematic dependence of the zonally averaged $\delta^{30}\text{Si}_{\text{sed}}$ anomaly on fertilization amplitude. For the HYPR case, the sediments south of $\sim 40^\circ\text{S}$ become progressively heavier with fertilization, saturating at an anomaly of about +0.3‰ around 50°S . Elsewhere, the sediments of the HYPR case become isotopically lighter with greatest anomalies in the subtropical gyres where the anomalies reach about -0.4‰ at the highest perturbation amplitude. For the EXP1 case, the subantarctic sediments become isotopically lighter, as does the rest of the ocean. The EXP1 $\delta^{30}\text{Si}_{\text{sed}}$ anomalies saturate for SO DFe $\geq 0.35\text{ nM}$, with the largest zonal-mean anomalies of about -1.0‰ at 40°S and of about -0.7‰ in the Northern Hemisphere

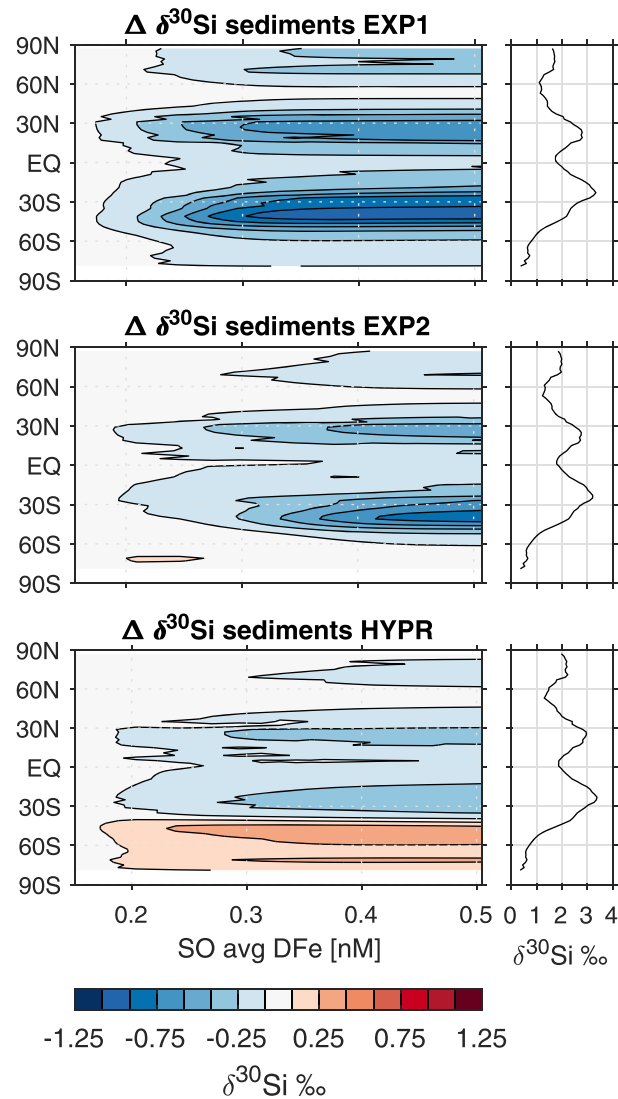


Figure 12. Anomalies in the zonally averaged $\delta^{30}\text{Si}$ of the opal flux onto the sediments as a function of SO DFe. The unperturbed base-state zonal averages are shown as line plots.

subtropics. The EXP2 case is similar to HYPR for SO DFe ≤ 0.3 nM but then behaves like EXP1 with further increasing SO DFe.

5. Discussion and Conclusions

We used a data-constrained model of the global coupled Si-P-Fe cycles in the modern ocean to explore the impact of differences in diatom physiology on the response to idealized Southern Ocean iron fertilization. Diatom physiology was parameterized in terms of the iron dependence of the Si:P uptake ratio $R^{\text{Si:P}}$ and the diatom growth rate $U_{\text{dia}}^{\text{P}}$. For conceptual simplicity, we considered two cases where $R^{\text{Si:P}}$ has exponential DFe dependence (EXP1 and EXP2) as well as the original $R^{\text{Si:P}}$ with hyperbolic DFe dependence (HYPR) used by Pasquier and Holzer (2017). With optimized parameters, all three cases have very similar unperturbed base states that match the observed nutrient climatology equally well.

The numerical efficiency of our model allowed us to systematically map out the steady-state nutrient cycles as a function of iron fertilization amplitude. The EXP1 case increased silicic acid leakage even for small-amplitude perturbations, while the EXP2 case increased leakage only for SO DFe ≥ 0.3 nM. In the HYPR case, $R^{\text{Si:P}}$ does not decrease sharply enough with increasing DFe to overwhelm fertilized diatom growth and enhance silicic acid leakage regardless of perturbation amplitude.

In the literature, silicic acid leakage is typically discussed by comparing the Si:N uptake ratio to the Si:N ratio of the nutrients supplied by the ambient water (e.g., Brzezinski et al., 2002), suggesting that for leakage to strengthen, iron fertilization should drive down the Si:N uptake ratio to match the Si:N supply ratio. However, strengthened silicic acid leakage can occur well before this condition is achieved—all that is necessary is that iron fertilization leads to a fractional decrease in $R^{\text{Si:P}}$ that exceeds the fractional increase in diatom growth, $U_{\text{dia}}^{\text{P}}$. The competing changes in $R^{\text{Si:P}}$ and $U_{\text{dia}}^{\text{P}}$ that occur for a given level of fertilization depend on the iron dependence of both factors.

In the formulation of Pasquier and Holzer (2017), the specific diatom growth rate μ_{dia} (the growth rate per unit of utilized phosphorus, an inverse time) is equal to the specific mortality rate in steady state and depends linearly on the diatom concentration p_{dia} . Because the diatom growth rate $U_{\text{dia}}^{\text{P}} = p_{\text{dia}} \mu_{\text{dia}}$ (mol P per unit volume per unit time), $U_{\text{dia}}^{\text{P}}$ is quadratic in the light and nutrient limitation terms $F_{\text{I,dia}}$ and $F_{\text{N,dia}}$ as in equation (1). One could argue for a different dependence of the specific mortality rate, and hence of μ_{dia} , on p_{dia} . For example, Dunne et al. (2005) chose the specific mortality rate of their large class to be proportional to p_{dia}^{α} , and Galbraith et al. (2010) take $\alpha = 1/3$ for numerical convenience (in our formulation, $\alpha = 1$). Choosing $\alpha \neq 1$ results in $U_{\text{dia}}^{\text{P}}$ being proportional to $(F_{\text{I,dia}} F_{\text{N,dia}})^{\alpha}$, where $\alpha = 1 + 1/\alpha$. For a given functional form of $R^{\text{Si:P}}$, these details merely change the threshold for leakage. Specifically, for exponential $R^{\text{Si:P}}$ and macronutrient-replete conditions, the factor of $\chi_{\text{Fe}}/2$ in the threshold e -folding DFe concentration χ_0 of equation (7) becomes χ_{Fe}/α . Thus, for $\alpha > 2$ (i.e., $\alpha < 1$) there would be increased sensitivity of silicic acid leakage to changing DFe compared to the case of $\alpha = 2$ considered here.

Interestingly, in iron-limited regions such as the Southern Ocean, the leakage threshold is relatively insensitive to the iron half-saturation constant k_{Fe} of diatoms. This is because under iron-limited conditions ($\chi_{\text{Fe}} \ll k_{\text{Fe}}$), the iron Monod term is in its linear regime so that the fractional change in diatom growth, $\delta U_{\text{dia}}^{\text{P}}/U_{\text{dia}}^{\text{P}}$ due to changes in iron concentration χ_{Fe} is independent of k_{Fe} . This is reflected in expression (7) of the threshold e -folding concentration χ_0 , where k_{Fe} enters through the $(1 + \chi_{\text{Fe}}/k_{\text{Fe}})$ correction term.

In principle the light-limitation term $F_{\text{I,c}}$ also has explicit DFe dependence that could influence the detailed response to iron fertilization. Here we parameterized $F_{\text{I,c}}$ as a simple Monod factor in the irradiance with a half-saturation constant that does not depend on DFe. More detailed parameterizations (e.g., Galbraith et al., 2010) include empirical DFe dependences in the light-limitation parameters. However, in these more complicated schemes, the overall dependence of growth rate on irradiance, DFe, and macronutrients is similar to the one employed here. While $F_{\text{I,c}}$ with explicit DFe dependence would modify the numerical value of the threshold e -folding scale χ_0 required for leakage, this would very likely be a second-order effect, and it would have no bearing on the simple mechanism of competition between $R^{\text{Si:P}}$ and $U_{\text{dia}}^{\text{P}}$.

We have quantified the strength of silicic acid leakage using the Southern Ocean trapping efficiency, which for the most strongly leaking EXP1 case at the highest perturbation amplitude is reduced to $\sim 32\%$ from an unperturbed value of $\sim 43\%$. For all Si:P cases, the phosphate trapping efficiency increases to $\sim 38\%$ at the highest perturbation amplitude from an unperturbed value of $\sim 26\%$. The corresponding decreases in opal export and increases in phosphorus export are reflected in a decrease of the silicon pump efficiency from 65% to 55%, and in an increase of the usual biological (phosphorus) pump efficiency from roughly 43% to 52%. In all cases, $R^{\text{Si:P}}$ decreases with increasing iron fertilization, leading to more efficient phosphorus export per mole of biogenic silica, thus increasing the diatom fraction of the global phosphorus export.

In response to enhanced silicic acid leakage at the highest fertilization rate (SO DFe ~ 0.5 nM), surface $\text{Si}(\text{OH})_4$ increases in the Southern Ocean by roughly 15–20 μM , in the Atlantic and Indian Ocean by 5–10 μM , and in the Pacific subtropical gyres by less than ~ 0.5 μM . These increases are sufficient to drive the silicic acid Monod factor of diatom growth above 0.5 everywhere except in the Pacific subtropical gyres. At this fertilization rate, colimitation with silicic acid is replaced by phosphate limitation or phosphate-iron colimitation in the Atlantic and Indian Oceans, and the silicic acid colimited regions of the Pacific subtropical gyres contract at their poleward and equatorial flanks.

The biomass response of all phytoplankton classes is largest in the Southern Ocean, with zonal-mean increases between roughly 50% and 70% at SO DFe ~ 0.5 nM, regardless of Si:P parameterization. For diatoms, the Southern Ocean biomass response dominates, and low-latitude increases driven by silicic acid leakage are an order of magnitude smaller. For the pico and nano phytoplankton classes, the low-latitude zonal-mean biomasses decrease by 10% to 30% for all Si:P cases in response to increased Southern Ocean

phosphate trapping. Shifts in community composition are largest in the subtropics, where silicic acid leakage and increased phosphate trapping drive order-0.1 increases in the diatom fraction. In the Pacific, these floristic shifts are driven primarily by increased diatom biomass; elsewhere attenuation of the nondiatom classes plays an equally important or dominant role.

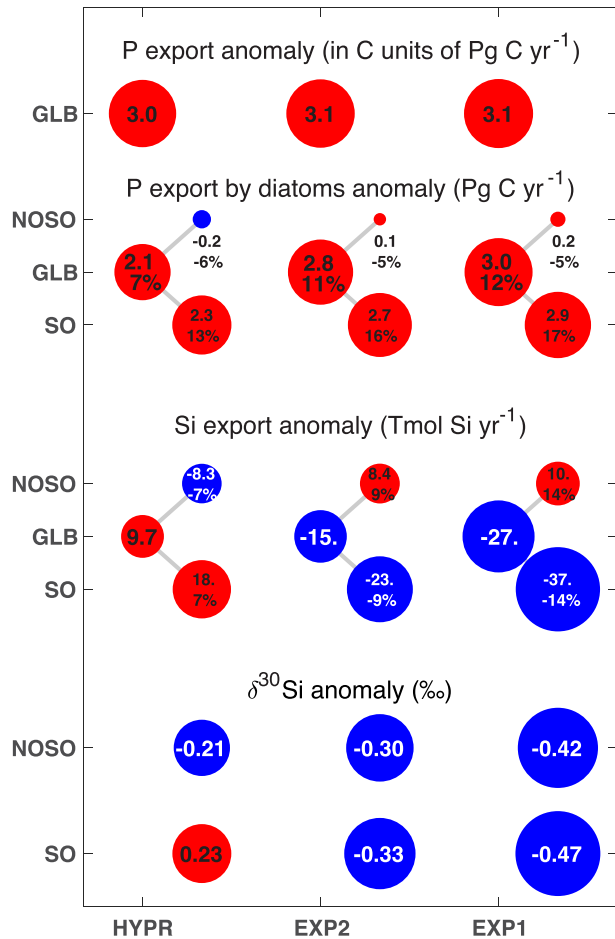


Figure 13. Summary of the key responses to Southern Ocean iron fertilization for SO DFe = 0.5 nM and the three Si:P cases considered (HYPR, EXP2, and EXP1, ordered from strongest silicic acid trapping to strongest leakage). Responses are shown as anomalies in the global phosphorus export Φ_P (converted to carbon units using C:P = 106:1), the global phosphorus export due to diatoms $\Phi_{P, \text{dia}}$, the global opal export Φ_{Si} , and the $\delta^{30}\text{Si}$ value of the opal flux onto the sediments averaged over the Southern Ocean (SO) and its global complement (north of Southern Ocean, NOSO). The anomalies of the diatom P and Si exports are partitioned into their SO and NOSO components, Φ^{SO} and Φ^{NOSO} . The percentages indicate the anomalies in the fractional contributions to the global exports from the SO and NOSO, that is, $\Delta(\Phi_{P, \text{dia}}^{\text{SO}}/\Phi_P)$ and $\Delta(\Phi_{P, \text{dia}}^{\text{NOSO}}/\Phi_P)$ as well as $\Delta(\Phi_{\text{Si}}^{\text{SO}}/\Phi_{\text{Si}})$ and $\Delta(\Phi_{\text{Si}}^{\text{NOSO}}/\Phi_{\text{Si}})$.

Figure 13 summarizes our key findings and illustrates them for the largest iron fertilization rate explored (SO DFe \sim 0.5 nM). At this level of fertilization, global organic matter export increases by about 3 Pg C/yr regardless of the $R^{\text{Si:P}}$ parameterization. The absolute percent contribution of diatoms to the global carbon export increases by 7% to 12%, with diatoms accounting for 47% to 59% of the total carbon export across the three Si:P cases (cf. Figure 8b). For EXP2 and the most strongly leaking EXP1 case, the increased diatom carbon export utilizes so much less of the available silicic acid that the global opal export drops by 15 and 27 Tmol Si/yr, respectively. For the HYPR case, fertilized diatom growth wins over reduced silicon requirement causing reduced silicic acid leakage and low-latitude opal export while Southern Ocean opal export increases for an overall global increase of 9.7 Tmol Si/yr.

Even with strengthened silicic acid leakage, the Southern Ocean dominates the response to Southern Ocean iron fertilization. Although the increased supply of silicic acid to low latitudes relieves Si colimitation over large regions and drives a subtropical floristic shift in favor of diatoms, the concurrently increased phosphate deficiency due to strengthened Southern Ocean phosphorus trapping and the remaining iron limitation north of the Southern Ocean (NOSO) limit the export response by diatoms. The NOSO organic matter export by diatoms barely responds to Southern Ocean iron fertilization so that the NOSO fraction of the global phosphorus export actually decreases by \sim 5% (Figure 13). However, increased silicic acid supply to low latitudes does increase the low-latitude opal export in spite of the overall Southern Ocean driven decrease in global opal export. At the highest fertilization rate and for the strongest silicic acid leakage (EXP1), the low latitudes export an additional \sim 10 Tmol Si/yr, which corresponds to a 14% increase in the NOSO fraction of the global opal export.

Differences in the DFe dependence of $R^{\text{Si:P}}$ impart distinct responses to the $\delta^{30}\text{Si}$ isotope signature of the opal flux. Strengthened silicic acid leakage (EXP1 and EXP2) extracts the heavier Si isotopes from the Southern Ocean in the form of preformed silicic acid (Holzer & Brzezinski, 2015), resulting in isotopically lighter opal flux throughout most of the oceans. By contrast, the increased Southern Ocean silicic acid trapping of the HYPR case produces isotopically heavier opal sediments in the Southern Ocean and lighter sediments elsewhere. As a result, the $\delta^{30}\text{Si}$ anomaly of the opal flux averaged over the Southern Ocean correlates with the global opal export anomaly.

Finally, we used the same data-assimilated modern ocean circulation model throughout, precluding quantitative comparisons with the paleo record. Nevertheless, it is interesting to note that measurements of sediment cores from the Southern Ocean (Beucher et al., 2007; De La Rocha et al., 1998; Horn et al., 2011; Robinson et al., 2014) consistently show lower $\delta^{30}\text{Si}$ during glacial periods, when iron inputs were presumably higher than during the Holocene (Andersen et al., 1998; Mahowald et al., 1999). This is broadly consistent with the $\delta^{30}\text{Si}$ response of the Si:P cases for which iron fertilization drives enhanced silicic acid leakage. Thus, while the available field and laboratory data for the Si:N uptake ratio has too much scatter to single out one of the parameterizations as being the most realistic, and all three Si:P parameterizations allow equally good fits to the current nutrient climatologies, the $\delta^{30}\text{Si}$ response argues that the EXP1 and

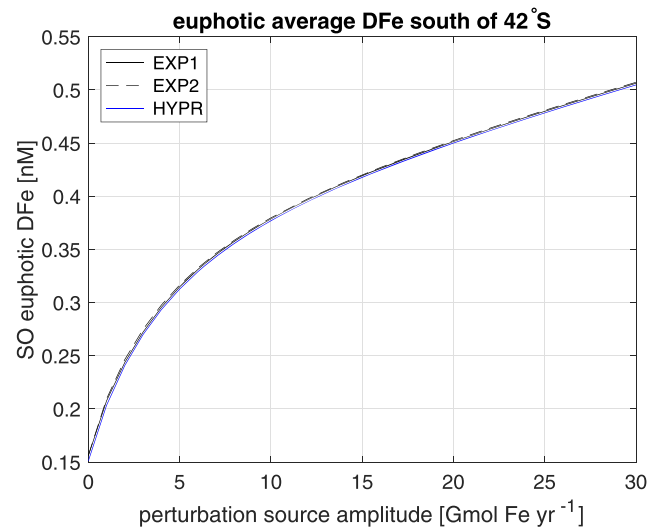


Figure A1. The euphotic-zone DFe concentration averaged over the Southern Ocean (south of 42°S) as a function of the strength of the additional Southern Ocean iron source.

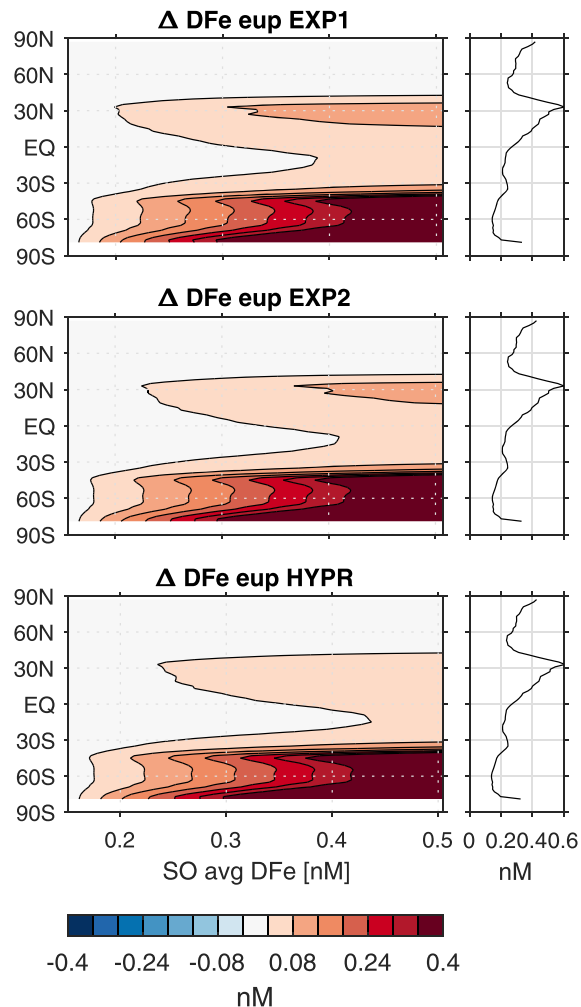


Figure A2. Zonally averaged euphotic-zone DFe concentrations as a function of SO DFe. The contoured plots are the anomalies from the base state shown in the line plots to the right.

EXP2 cases are more realistic than the HYPR case. Our results underscore the importance of constraining the iron dependence of the diatom Si:N uptake ratio, and of accurately representing this dependence in ocean biogeochemical models, not only to assess the SALH but also to predict the future response of ocean productivity to changes in iron cycling (e.g., Moore et al., 2018). In future work, we plan to investigate the role of circulation changes (e.g., Crosta et al., 2007) in controlling silicic acid leakage and its Si isotopic signature.

Appendix A: Surface DFe Response to Iron Fertilization

Figure A1 shows SO DFe, defined as the DFe concentration averaged over the Southern Ocean euphotic zone (upper 73 m south of 42°S), as a function of the rate with which additional iron is dissolved uniformly in the Southern Ocean surface layer. The response of the DFe field to iron fertilization is nearly identical for all three Si:P parameterizations. The zonally averaged euphotic-zone DFe anomaly as a function of SO DFe is plotted in Figure A2. DFe in the euphotic zone increases most in the Southern Ocean but the response extends well into the Northern Hemisphere (NH) where the largest increases occur in the North Atlantic subtropical gyre. All three Si:P cases have a very similar response, although the NH DFe anomaly is larger for EXP1 and EXP2 than for HYPR.

Appendix B: Iron Dependence of Si:P Uptake Ratio Compared to Observations

Field and laboratory data for the Si:N uptake ratio of diatoms are plotted in Figure B1. The field data from Hutchins and Bruland (1998) (blue symbols) and Franck et al. (2000) (black symbols) were obtained from incubations of seawater samples, taken from California and Southern Ocean waters, respectively, and hence represent community uptake. The data from Timmermans et al. (2004) (red symbols) is from laboratory

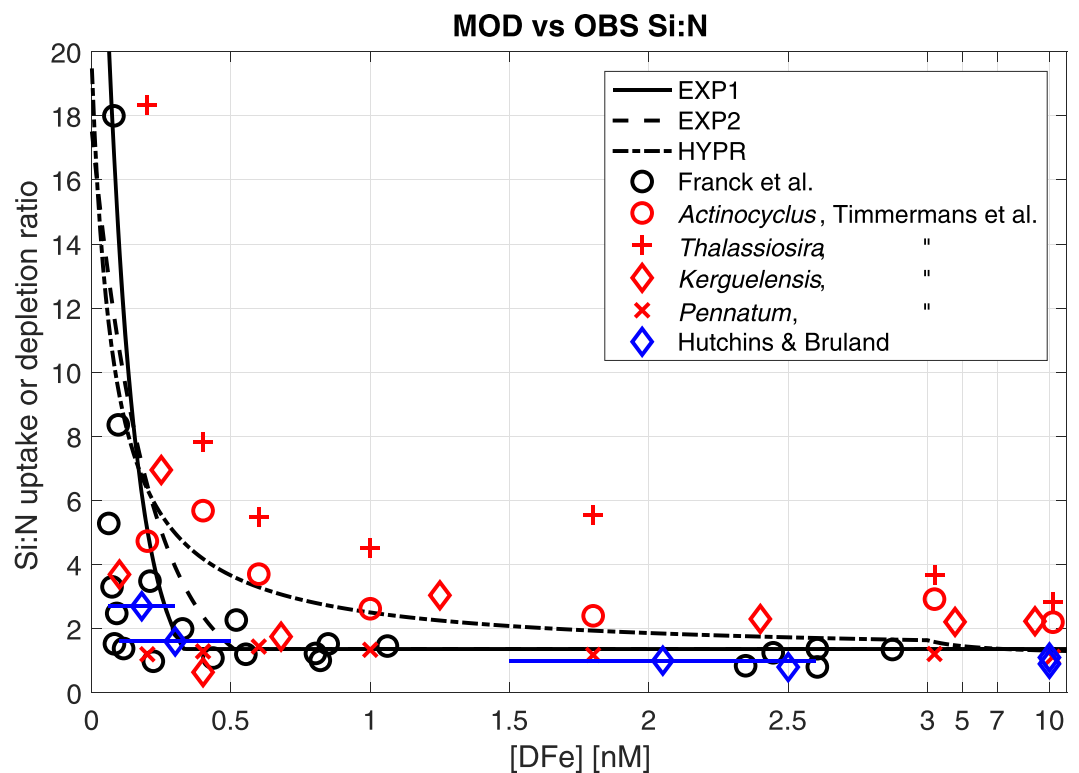


Figure B1. Observed Si:N uptake ratio as a function of dissolved iron concentration compared to our three model parameterizations of the Si:P uptake ratio converted to Si:N using N:P = 11:1. The black symbols are field data from Franck et al. (2000) (also reported by Brzezinski et al., 2002, with an additional data point), the red data are species-specific depletion ratios as reported by Timmermans et al. (2004), and the blue data are from the study by Hutchins and Bruland (1998). (The horizontal blue lines indicate the reported uncertainty in the DFe concentration.) The model curves are plotted for silicic acid-replete conditions. Note the change in DFe scale for [DFe] > 3 nM.

cultures of four specific diatom species grown in filtered seawater collected in the Southern Ocean. For comparison with our parameterizations of the Si:P uptake ratio, the field data would ideally represent community uptake ratios of diatoms only. However, the nitrate uptake of the field data is due to all phytoplankton in the sample and the Si:N uptake ratio could thus be underestimated because of nondiatom nitrate uptake, or perhaps even overestimated if some of the diatom nitrate requirement is provided by ammonium uptake, which was not measured. The species-specific data of Timmermans et al. (2004) shows considerable variation among different diatom species and it is unclear how to average them to get an Si:N uptake ratio representative of the diatom communities present in seawater.

The model curves (Si:P converted with N:P = 11:1) match the iron-replete limit ($[DFe] \gtrsim 1$ nM) reasonably well, though there is a great deal of scatter even in this limit. Arguably, the EXP1 curve matches the field data (blue and black symbols) at the lowest measured DFe concentrations best. The HYPR curve is closest to the *Actinocyclus* and *Thalassiosira* culture data. In the absence of other information (e.g., the Si isotope response to iron fertilization considered here) it would be difficult to choose any of our Si:P uptake ratios as being the most realistic. We emphasize that none of the model curves were formally fit to any of these data, but were selected based on theoretical considerations as described in section 3.

Appendix C: Diatom Nutrient Limitation Patterns

Figure C1 shows the nutrient limitation patterns of diatoms in the unperturbed states and in the iron-fertilized states corresponding to SO DFe ~ 0.5 nM. These patterns are defined following Pasquier and Holzer (2017) in terms of the nutrient concentration χ_n (for nutrient n) relative to the half-saturation constant $k_{n,c}$ of the nutrient for phytoplankton class c : We deem nutrient n to be limiting class c if $\chi_n/k_{n,c} < 1/2$. Because we have three nutrients, we can define limitation in terms of an RGB color ($D_c^P, D_c^{Si}, D_c^{Fe}$), where the $D_c^n \equiv 1 - \chi_n/(\chi_n + k_{n,c})$ is the deficiency of class c in nutrient n . Because the continuous colors make it

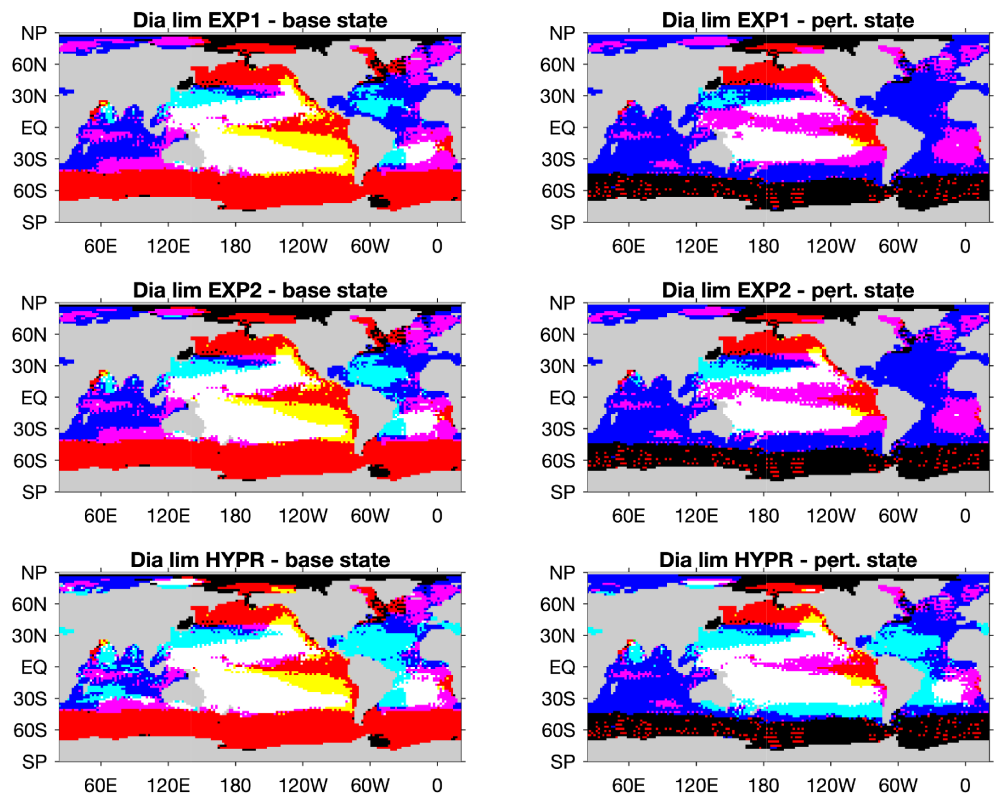


Figure C1. Maps of the nutrient limitation patterns for the unperturbed base states (left) and for the Southern Ocean iron-fertilized states at SO DFe ~ 0.5 nM (right). The colors are defined as described in Appendix C and indicate the following: red is Fe limitation, blue is P limitation, green is Si limitation, magenta is Fe-P colimitation, cyan is Si-P colimitation, and yellow is Fe-Si colimitation. Black indicates repleteness in all three nutrients, and white indicates deficiency in all three nutrients.

difficult to discern patterns, we use discretized colors ($L_c^P, L_c^{Si}, L_c^{Fe}$), where $L_c^n = 1$ if $D_c^n > 1/2$ (equivalently $\chi_n/k_{n,c} < 1/2$), and $L_c^n = 0$ otherwise. Thus, with only a single nutrient falling below the half-saturation constant, red (1, 0, 0) is iron limitation, green (0, 1, 0) is Si limitation, and blue (0, 0, 1) is P limitation. If two nutrients fall below half saturation, magenta (1, 0, 1) indicates Fe-P colimitation, yellow (1, 1, 0) indicates Fe-Si colimitation, and cyan (0, 1, 1) indicates Si-P colimitation. If none of the nutrients fall below half-saturation, we obtain black (0, 0, 0), and if all nutrients fall below half-saturation, we obtain white (1, 1, 1).

Acknowledgments

M. H. acknowledges the hospitality of the UCSB Earth Research Institute where much of this work was done. B. P. acknowledges postdoctoral support from UC Irvine through DOE Grant DE-SC0016539 (J. K. Moore) and NSF Grant OCE-1658380 (J. K. Moore and F. Primeau). T. D. acknowledges support from NSF Grant OCE-1658392. M. B. acknowledges support from NSF Grant OCE-1732139. The data against which our model was optimized are available as follows: phosphate and silicic acid data from www.nodc.noaa.gov/OC5/woa13/woa13data.html, dissolved iron data from www.bodc.ac.uk/geotraces/data, and satellite estimates of plankton concentrations from [doi:10.1594/PANGAEA.859005](https://doi.org/10.1594/PANGAEA.859005). Annual PAR irradiance data is available online (from <https://oceancolor.gsfc.nasa.gov>).

References

- Andersen, K. K., Armengaud, A., & Genthon, C. (1998). Atmospheric dust under glacial and interglacial conditions. *Geophysical Research Letters*, *25*, 2281–2284.
- Arellano-Torres, E., Pichevin, L. E., & Ganeshram, R. S. (2011). High-resolution opal records from the eastern tropical Pacific provide evidence for silicic acid leakage from HNLC regions during glacial periods. *Quaternary Science Reviews*, *30*, 1112–1121. <https://doi.org/10.1016/j.quascirev.2011.02.002>
- Assmy, P., Smetacek, V., Montresor, M., Klaas, C., Henjes, J., Strass, V. H., et al. (2013). Thick-shelled, grazer-protected diatoms decouple ocean carbon and silicon cycles in the iron-limited antarctic circumpolar current. *Proceedings of the National Academy of Sciences of the United States of America*, *110*, 20,633–20,638. <https://doi.org/10.1073/pnas.1309345110>
- Aumont, O., Maier-Reimer, E., Blain, S., & Monfray, P. (2003). An eco-system model of the global ocean including Fe, Si, P colimitations. *Global Biogeochemical Cycles*, *17*(2), 1060. <https://doi.org/10.1029/2001GB001745>
- Beucher, C. P., Brzezinski, M. A., & Crosta, X. (2007). Silicic acid dynamics in the glacial subantarctic: Implications for the silicic acid leakage hypothesis. *Global Biogeochemical Cycles*, *21*, GB3105. <https://doi.org/10.1029/2006GB002746>
- Bradtmiller, L. I., Anderson, R. F., Fleisher, M. Q., & Burckle, L. H. (2006). Diatom productivity in the equatorial Pacific Ocean from the last glacial period to the present: A test of the silicic acid leakage hypothesis. *Paleoceanography*, *21*, PA4201. <https://doi.org/10.1029/2006pa001282>
- Bradtmiller, L. I., Anderson, R. F., Fleisher, M. Q., & Burckle, L. H. (2007). Opal burial in the equatorial Atlantic Ocean over the last 30 ka: Implications for glacial-interglacial changes in the ocean silicon cycle. *Paleoceanography*, *22*, PA4216. <https://doi.org/10.1029/2007PA001443>
- Brzezinski, M. A. (1985). The Si:C:N ratio of marine diatoms: Interspecific variability and the effect of some environmental variables. *Journal of Phycology*, *21*, 347–357.
- Brzezinski, M. A., Pride, C. J., Franck, V. M., Sigman, D. M., Sarmiento, J. L., Matsumoto, K., et al. (2002). A switch from $\text{Si}(\text{OH})_4$ to NO_3^- depletion in the glacial Southern Ocean. *Geophysical Research Letters*, *29*(12), 1564. <https://doi.org/10.1029/2001GL014349>
- Crosta, X., Beucher, C., Pahnke, K., & Brzezinski, M. A. (2007). Silicic acid leakage from the Southern Ocean: Opposing effects of nutrient uptake and oceanic circulation. *Geophysical Research Letters*, *34*, L13601. <https://doi.org/10.1029/2006GL029083>
- De La Rocha, C. L., Brzezinski, M. A., DeNiro, M. J., & Shemesh, A. (1998). Silicon-isotope composition of diatoms as an indicator of past oceanic change. *Nature*, *395*, 680–683.
- Dubois, N., Kienast, M., Kienast, S., Calvert, S. E., Francois, R., & Anderson, R. F. (2010). Sedimentary opal records in the eastern equatorial Pacific: It is not all about leakage. *Global Biogeochemical Cycles*, *24*, GB4020. <https://doi.org/10.1029/2010GB003821>
- Dunne, J. P., Armstrong, R. A., Gnanadesikan, A., & Sarmiento, J. L. (2005). Empirical and mechanistic models for the particle export ratio. *Global Biogeochemical Cycles*, *19*, GB4006. <https://doi.org/10.1029/2004gb002390>
- Franck, V. M., Brzezinski, M. A., Coale, K. H., & Nelson, D. M. (2000). Iron and silicic acid concentrations regulate Si uptake north and south of the Polar Frontal Zone in the Pacific sector of the Southern Ocean. *Deep-Sea Research II*, *47*, 3315–3338.
- Galbraith, E. D., Gnanadesikan, A., Dunne, J. P., & Hiscock, M. R. (2010). Regional impacts of iron-light colimitation in a global biogeochemical model. *Biogeosciences*, *7*, 1043–1064. <https://doi.org/10.5194/bg-7-1043-2010>
- Galbraith, E. D., & Martiny, A. C. (2015). A simple nutrient-dependence mechanism for predicting the stoichiometry of marine ecosystems. *Proceedings of the National Academy of Sciences of the United States of America*, *112*, 8199–8204. <https://doi.org/10.1073/pnas.1423917112>
- Garcia, H. E., Locarnini, R. A., Boyer, T. P., Antonov, J. I., Baranova, O. K., Zweng, M. M., et al. (2014). World Ocean Atlas 2013. In S. Levitus (Ed.), *NOAA Atlas NESDIS 76, Volume 4: Dissolved Inorganic Nutrients (phosphate, nitrate, silicate)* (pp. 25). Silver Spring: A. Mishonov Technical Ed.
- Gnanadesikan, A. (1999). A global model of silicon cycling: Sensitivity to eddy parameterization and dissolution. *Global Biogeochemical Cycles*, *13*, 199–220.
- Griffiths, J. D., Barker, S., Hendry, K. R., Thornalley, D. J. R., van de Flierdt, T., Hall, I. R., & Anderson, R. F. (2013). Evidence of silicic acid leakage to the tropical Atlantic via Antarctic Intermediate Water during Marine Isotope Stage 4. *Paleoceanography*, *28*, 307–318. <https://doi.org/10.1002/palo.20030>
- Hendry, K. R., & Brzezinski, M. A. (2014). Using silicon isotopes to understand the role of the Southern Ocean in modern and ancient biogeochemistry and climate. *Quaternary Science Reviews*, *89*, 13–26. <https://doi.org/10.1016/j.quascirev.2014.01.019>
- Holzer, M., & Brzezinski, M. A. (2015). Controls on the silicon isotope distribution in the ocean: New diagnostics from a data-constrained model. *Global Biogeochemical Cycles*, *29*, 267–287. <https://doi.org/10.1002/2014GB004967>
- Holzer, M., & Primeau, F. W. (2013). Global teleconnections in the oceanic phosphorus cycle: Patterns, paths, and timescales. *Journal of Geophysical Research*, *118*, 1775–1796. <https://doi.org/10.1002/jgrc.20072>
- Holzer, M., Primeau, F. W., DeVries, T., & Matear, R. (2014). The Southern Ocean silicon trap: Data-constrained estimates of regenerated silicic acid, trapping efficiencies, and global transport paths. *Journal of Geophysical Research: Oceans*, *119*, 313–331. <https://doi.org/10.1002/2013JC009356>
- Horn, M. G., Beucher, C. P., Robinson, R. S., & Brzezinski, M. A. (2011). Southern Ocean nitrogen and silicon dynamics during the last deglaciation. *Earth and Planetary Science Letters*, *310*, 334–339.
- Hutchins, D. A., & Bruland, K. W. (1998). Iron-limited diatom growth and Si:N uptake ratios in a coastal upwelling regime. *Nature*, *393*, 561–564. <https://doi.org/10.1038/31203>
- Ito, T., & Follows, M. J. (2005). Preformed phosphate, soft tissue pump and atmospheric CO_2 . *Journal of Marine Research*, *63*, 813–839.

- Kienast, S. S., Kienast, M., Jaccard, S., Calvert, S. E., & Francois, R. (2006). Testing the silica leakage hypothesis with sedimentary opal records from the eastern equatorial Pacific over the last 150 kyrs. *Geophysical Research Letters*, *33*, L15607. <https://doi.org/10.1029/2006GL026651>
- Kostadinov, T. S., Milutinović, S., Marinov, I., & Cabré, A. (2016). Carbon-based phytoplankton size classes retrieved via ocean color estimates of the particle size distribution. *Ocean Science*, *12*(2), 561–575. <https://doi.org/10.5194/os-12-561-2016>
- Mahowald, N., Kohfeld, K., Hansson, M., Balkanski, Y., Harrison, S. P., Prentice, I. C., et al. (1999). Dust sources and deposition during the Last Glacial Maximum and current climate: A comparison of model results with paleodata from ice cores and marine sediments. *Journal of Geophysical Research*, *104*, 15,895–15,916.
- Maier, E., Méheust, M., Abelmann, A., Gersonde, R., Chaplignin, B., Ren, J., et al. (2015). Deglacial subarctic Pacific surface water hydrography and nutrient dynamics and links to North Atlantic climate variability and atmospheric CO₂. *Paleoceanography*, *30*, 949–968. <https://doi.org/10.1002/2014PA002763>
- Marchetti, A., & Harrison, P. J. (2007). Coupled changes in the cell morphology and the elemental (C, N, and Si) composition of the pennate diatom *Pseudo-nitzschia* due to iron deficiency. *Limnology and Oceanography*, *52*, 2270–2284.
- Marchetti, A., Varela, D. E., Lance, V. P., Johnson, Z., Palmucci, M., Giordano, M., & Armbrust, E. V. (2010). Iron and silicic acid effects on phytoplankton productivity, diversity, and chemical composition in the equatorial Pacific Ocean. *Limnology and Oceanography*, *55*, 11–29.
- Matsumoto, K., Chase, Z., & Kohfeld, K. (2014). Different mechanisms of silicic acid leakage and their biogeochemical consequences. *Paleoceanography*, *29*, 238–254. <https://doi.org/10.1002/2013PA002588>
- Matsumoto, K., & Sarmiento, J. L. (2008). A corollary to the silicic acid leakage hypothesis. *Paleoceanography*, *23*, PA2203. <https://doi.org/10.1029/2007PA001515>
- Matsumoto, K., Sarmiento, J. L., & Brzezinski, M. A. (2002). Silicic acid leakage from the Southern Ocean: A possible explanation for glacial atmospheric pCO₂. *Global Biogeochemical Cycles*, *16*(3), 1031. <https://doi.org/10.1029/2001GB001442>
- Matsumoto, K., Tokos, K., Huston, A., & Joy-Warren, H. (2013). MESMO 2: A mechanistic marine silica cycle and coupling to a simple terrestrial scheme. *Geoscientific Model Development*, *6*(2), 477–494. <https://doi.org/10.5194/gmd-6-477-2013>
- Matsumoto, K., Tokos, K. S., Price, A. R., & Cox, S. J. (2008). First description of the Minnesota Earth System Model for ocean biogeochemistry (MESMO, 1.0). *Geoscientific Model Development*, *1*, 1–15. <https://doi.org/10.5194/gmd-1-1-2008>
- Mawji, E., Schlitzer, R., Dodas, E. M., Abadie, C., Abouchami, W., Anderson, R. F., et al. (2015). The GEOTRACES Intermediate Data Product 2014. *Marine Chemistry*, *177*, 1–8. <https://doi.org/10.1016/j.marchem.2015.04.005> Biogeochemistry of trace elements and their isotopes.
- Moore, J. K., Doney, S. C., & Lindsay, K. (2004). Upper ocean ecosystem dynamics and iron cycling in a global three-dimensional model. *Global Biogeochemical Cycles*, *18*, GB4028. <https://doi.org/10.1029/2004GB002220>
- Moore, J. K., Fu, W., Primeau, F., Britten, G. L., Lindsay, K., Long, M., et al. (2018). Sustained climate warming drives declining marine biological productivity. *Science*, *359*, 1139–1143. <https://doi.org/10.1126/science.aao6379>
- Moore, C. M., Mills, M. M., Arrigo, K. R., Berman-Frank, I., Bopp, L., Boyd, P. W., et al. (2013). Processes and patterns of oceanic nutrient limitation. *Nature Geoscience*, *6*, 701–710. <https://doi.org/10.1038/NGE01765>
- Nelson, D. M., Tréguer, P., Brzezinski, M. A., Leynaert, A., & Quéruiner, B. (1995). Production and dissolution of biogenic silica in the ocean: Revised global estimates, comparison with regional data and relationship to biogenic sedimentation. *Global Biogeochemical Cycles*, *9*, 359–372.
- Nozaki, Y., & Yamamoto, Y. (2001). Radium 228 based nitrate fluxes in the eastern Indian Ocean and the South China Sea and a silicon-induced “alkalinity pump” hypothesis. *Global Biogeochemical Cycles*, *15*, 555–567. <https://doi.org/10.1029/2000GB001309>
- Paasche, E. (1973). Silicon and the ecology of marine planktonic diatoms. I. *Thalassiosira pseudonana* (Cyclotella nana) grown in chemostats with silicate as the limiting nutrient. *Marine Biology*, *19*, 117–126. <https://doi.org/10.1007/BF00353582>
- Pasquier, B., & Holzer, M. (2017). Inverse-model estimates of the ocean's coupled phosphorus, silicon, and iron cycles. *Biogeosciences*, *14*(18), 4125–4159. <https://doi.org/10.5194/bg-14-4125-2017>
- Pasquier, B., & Holzer, M. (2018). The number of past and future regenerations of iron in the ocean and its intrinsic fertilization efficiency. *Biogeosciences*, *15*, 7177–7203. <https://doi.org/10.5194/bg-15-7177-2018>
- Pichevin, L. E., Reynolds, B. C., Ganeshram, R. S., Cacho, I., Pena, L., Keefe, K., & Ellam, R. M. (2009). Enhanced carbon pump inferred from relaxation of nutrient limitation in the glacial ocean. *Nature*, *459*, 1114–1118. <https://doi.org/10.1038/nature08101>
- Primeau, F. W., Holzer, M., & DeVries, T. (2013). Southern Ocean nutrient trapping and the efficiency of the biological pump. *Journal of Geophysical Research*, *118*, 2547–2564. <https://doi.org/10.1002/jgrc.20181>
- Quigg, A., Finkel, Z. V., Irwin, A. J., Rosenthal, Y., Ho, T.-Y., Reinfelder, J. R., et al. (2003). The evolutionary inheritance of elemental stoichiometry in marine phytoplankton. *Nature*, *425*, 291–294. <https://doi.org/10.1038/nature01953>
- Robinson, R. S., Brzezinski, M. A., Beucher, C., Horn, M. G. S., & Bedsole, P. (2014). The changing roles of iron and vertical mixing in regulating nitrogen and silicon cycling in the Southern Ocean over the last glacial cycle. *Paleoceanography*, *29*, 1179–1195. <https://doi.org/10.1029/2018GB006045>
- Roshan, S., DeVries, T., Wu, J., & Chen, G. (2018). The internal cycling of zinc in the ocean. *Global Biogeochemical Cycles*, *32*, 1833–1849. <https://doi.org/10.1029/2018GB006045>
- Saito, M. A., Goepfert, T. J., & Ritt, J. T. (2008). Some thoughts on the concept of colimitation: Three definitions and the importance of bioavailability. *Limnology and Oceanography*, *53*, 276–290.
- Sarmiento, J. L., Gruber, N., Brzezinski, M. A., & Dunne, J. P. (2004). High-latitude controls of thermocline nutrients and low latitude biological productivity. *Nature*, *427*, 56–60.
- Tagliabue, A., Mtshali, T., Aumont, O., Bowie, A. R., Klunder, M. B., Roychoudhury, A. N., & Swart, S. (2012). A global compilation of dissolved iron measurements: Focus on distributions and processes in the Southern Ocean. *Biogeosciences*, *9*(6), 2333–2349. <https://doi.org/10.5194/bg-9-2333-2012>
- Takeda, S. (1998). Influence of iron availability on nutrient consumption ratio of diatoms in oceanic waters. *Nature*, *393*, 774–777. <https://doi.org/10.1038/31674>
- Timmermans, K. R., van der Wagt, B., & de Baar, H. J. W. (2004). Growth rates, half-saturation constants, and silicate, nitrate, and phosphate depletion in relation to iron availability of four large, open-ocean diatoms from the Southern Ocean. *Limnology and Oceanography*, *49*, 2141–2151. <https://doi.org/10.4319/lo.2004.49.6.2141>
- Tréguer, P. J. (2014). The Southern Ocean silica cycle. *Comptes Rendus Geoscience*, *346*, 279–286. <https://doi.org/10.1016/j.crte.2014.07.003>
- Uitz, J., Claustre, H., Gentili, B., & Stramski, D. (2010). Phytoplankton class-specific primary production in the world's oceans: Seasonal and interannual variability from satellite observations. *Global Biogeochemical Cycles*, *24*, GB3016. <https://doi.org/10.1029/2009GB003680>
- Weber, T. S., & Deutsch, C. (2010). Ocean nutrient ratios governed by plankton biogeography. *Nature*, *467*, 550–554. <https://doi.org/10.1038/nature09403>